Confined diffusion of transmembrane proteins and lipids induced by the same actin meshwork lining the plasma membrane

AUTHOR(S):

Fujiwara, T. K.; Iwasawa, K.; Kalay, Z.; Tsunoyama, T. A.; Watanabe, Y.; Umemura, Y. M.; Murakoshi, H.; ... Nemoto, Y. L.; Morone, N.; Kusumi, A.

京都大学学術情報リポジトリ

KURENAI

Kyoto University Research Information Repository

Confined diffusion of transmembrane proteins and lipids induced by the same actin meshwork lining the plasma membrane

Takahiro K. Fujiwara[a], Kokoro Iwasawa[b], Ziya Kalay[c], Taka A. Tsunoyama[c], Yusuke Watanabe[c], Yasuhiro M. Umemura[d], Hideji Murakoshi[e], Kenichi G. N. Suzuki[c,f], Yuri L. Nemoto[c], Nobuhiro Morone[g], and Akihiro Kusumi[b,c,h,*]

[a]Center for Meso-Bio Single-Molecule Imaging, Institute for Integrated Cell-Material Sciences, Kyoto 606-8501, Japan; [b]Institute for Frontier Medical Sciences, Kyoto University, Kyoto 606-8507, Japan; [c]Institute for Integrated Cell-Material Sciences, Kyoto 606-8507, Japan; [d]Department of Physiology and Systems Bioscience, Kyoto Prefectural University of Medicine, Kyoto 602-8566, Japan; [e]National Institute for Physiological Sciences, Okazaki 444-8585, Japan; [f]Institute for Stem Cell Biology and Regenerative Medicine and National Centre for Biological Sciences, Bangalore 650056, India; [g]MRC Toxicology Unit, University of Leicester, Leicester LE1 9HN, United Kingdom; [h]Membrane Cooperativity Unit, Okinawa Institute of Science and Technology, Onna-son, Okinawa 904-0412, Japan

ABSTRACT The mechanisms by which the diffusion rate in the plasma membrane (PM) is regulated remain unresolved, despite their importance in spatially regulating the reaction rates in the PM. Proposed models include entrapment in nanoscale noncontiguous domains found in PtK2 cells, slow diffusion due to crowding, and actin-induced compartmentalization. Here, by applying single-particle tracking at high time resolutions, mainly to the PtK2-cell PM, we found confined diffusion plus hop movements (termed "hop diffusion") for both a nonraft phospholipid and a transmembrane protein, transferrin receptor, and equal compartment sizes for these two molecules in all five of the cell lines used here (actual sizes were cell dependent), even after treatment with actin-modulating drugs. The cross-section size and the cytoplasmic domain size both affected the hop frequency. Electron tomography identified the actin-based membrane skeleton (MSK) located within 8.8 nm from the PM cytoplasmic surface of PtK2 cells and demonstrated that the MSK mesh size was the same as the compartment size for PM molecular diffusion. The extracellular matrix and extracellular domains of membrane proteins were not involved in hop diffusion. These results support a model of anchored TM-protein pickets lining actin-based MSK as a major mechanism for regulating diffusion.

INTRODUCTION

Reaction kinetics is central to cellular processes (Saxton, 1982; Kalay et al., 2012). In the cellular plasma membrane (PM), large spatiotemporal

variations in reaction kinetics, which might be important for regulating signal transduction in the PM, can be induced by the presence of a variety of dynamic mesoscale (3–300 nm) domains (Suzuki et al., 2007a,b; Costa et al., 2009, 2011; Chung et al., 2010; Treanor et al., 2010; Parton and del Pozo, 2013), as well as the active processes that transiently assemble actin filaments and the proteins interacting with them (Chaudhuri et al., 2011; Gowrishankar et al., 2012).

One of the most controversial issues about the domain structure of the plasma membrane is the actin-induced compartmentalization of the PM. Transmembrane (TM) proteins, phospholipids, and glycosylphosphatidylinositol (GPI)-anchored proteins have been proposed to undergo short-term confined diffusion within compartments of ~100 nm formed by the actin-filament meshwork bound to the PM inner surface (Morone et al., 2006), called the membrane-skeleton (MSK) fence, and various TM proteins lining the actin-based MSK, called anchored TM-protein pickets (Figure 1A; Kusumi et al.,
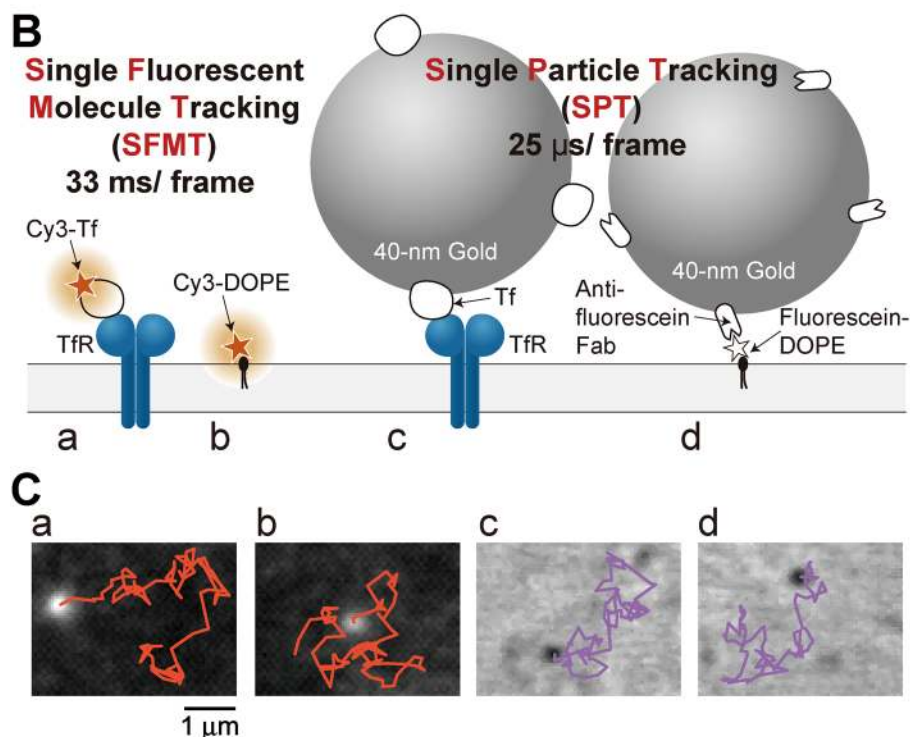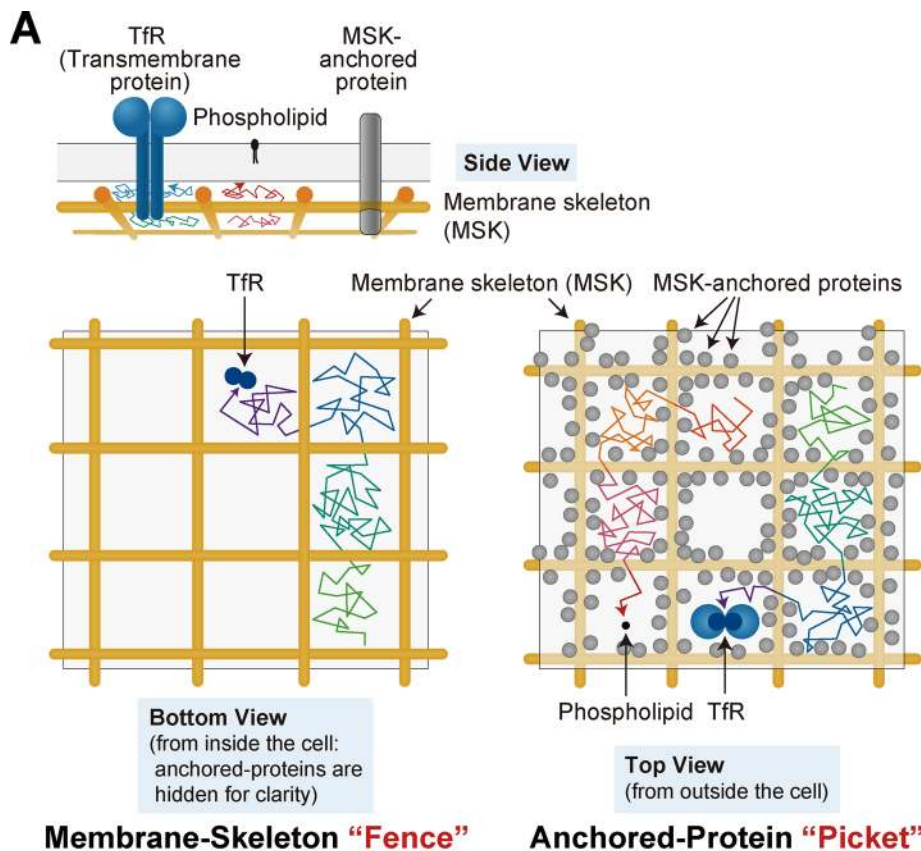
FIGURE 1: The MSK fence and anchored-TM-protein picket model, and the single-molecule tracking methods used in this study. (A) Fence-and-pickets model. The PM can be partitioned into compartments, and both TM proteins and lipids undergo short-term confined diffusion within a compartment and long-term hop movements between these compartments, which is termed hop diffusion. Temporary confinement within the compartment is induced by the actin-MSK "fences" and the anchored-TM-protein "pickets" anchored to and aligned along the

2005, 2012; Kalay *et al.*, 2014). Of importance, these pickets exert not only steric hindrance effects but also hydrodynamic friction effects on the surrounding molecules, thus inducing confining effects on membrane molecules. Membrane molecules undergo long-term hop movements between compartments, and the long-term macroscopic diffusion coefficients are reduced by a factor of ~20 from the microscopic diffusion coefficient within a compartment, which is comparable to the single diffusion coefficients found in the blebbed PM, where actin filaments are largely depleted, and in artificial lipid membranes (6–10 μm^2/s; Fujiwara *et al.*, 2002; Kusumi *et al.*, 2012).

The hop diffusion of TM proteins, such as the transferrin receptor (TfR), has been well established by many independent studies, including a fluorescence correlation spectroscopy (FCS) study by Lenne *et al.* (2006), and the MSK fence model for TM-protein hop diffusion has been widely accepted (Vereb *et al.*, 2003; Lenne *et al.*, 2006; Owen *et al.*, 2009; Jaqaman and Grinstein, 2012; Di Rienzo *et al.*, 2013; Nicolson, 2014). However, the hop diffusion of phospholipids (Fujiwara *et al.*, 2002; Murase *et al.*, 2004; Hiramoto-Yamaki *et al.*, 2014), glycosphingolipids (Day and Kenworthy, 2012), and GPI-anchored proteins (Umemura *et al.*, 2008; Klotzsch and Schütz, 2013), that is, that of the lipids and lipid-anchored molecules located

actin MSK. In this study, we examined the movements of DOPE and TfR (a native dimer). Side view, a variety of TM proteins (temporarily) bind to the MSK, and these MSK-anchored TM proteins act like "pickets." Bottom view, the PM cytoplasmic surface, viewed from inside the cell, showing the MSK "fence" model. Top view, many TM proteins are (temporarily) anchored to and aligned along the actin MSK, exerting hydrodynamic circumferential-slowing (enhanced viscosity) and steric-hindrance effects on PM molecules that approach the anchored TM-proteins. (B) Experimental design for SFMT and SPT. For SFMT, TfR tagged with Cy3-Tf (a) and Cy3-DOPE (b) were used. For SPT, TfR tagged with 40-nm-diameter colloidal gold particles coated with a small number of transferrin molecules were used (c). For colloidal-gold labeling of DOPE (d), gold probes coated with anti-fluorescein antibody Fab fragments were bound to fluorescein-conjugated DOPE, which was preincorporated in the PM. The fluorescein moiety was used as a tag for the antibody Fab rather than a fluorescent probe. (C) Images of Cy3 and colloidal-gold probes and their trajectories at video rate for 3 s, observed on the top surface of PtK2 cells. Here a–d are the same as in B.

in the PM outer leaflet, is controversial. One of the major reasons this problem has drawn strong attention involves its general interest. Phospholipids are the most fundamental molecular species to form the biological membrane; without them, biological membranes would not be generated. Therefore determining whether and how the dynamics of such fundamental molecular species is regulated in the PM is extremely important for understanding the dynamics of all membrane-associated molecules, as well as their functions enabled by such dynamics.

The other reason for interest in this problem, which is specific to the picket model, is that it has been difficult to examine directly the effects of rows of picket proteins anchored to and aligned along the actin-based MSK on the dynamics of other molecules in the PM. However, if the picket model were true, then the compartment size detected by phospholipids located in the PM outer leaflet would be the same as that detected by TM proteins.

Therefore the first objective of the present research was to examine the possible equality of the compartment sizes for a typical nonraft phospholipid, L-α-diolelylphosphatidylethanolamine (DOPE), and a TM protein, TfR. Furthermore, to establish the generality of the equal compartment size for DOPE and TfR, we examined the PMs of five cell lines, PtK2, normal rat kidney (NRK), T24, HeLa, and HEPA-OVA, both in the PMs of intact cells and in cells treated with actin-modifying drugs.

By using the PM of the PtK2 cell line and applying cutting-edge technologies such as (scanning) stimulated emission depletion–FCS (Eggeling *et al.*, 2009; Honigmann *et al.*, 2014) and simultaneous fluorescence signal detection on three closely arranged separate point detectors (Sahl *et al.*, 2010), it has been found that phospholipids, even nonraft phospholipids (Sezgin *et al.*, 2012; Honigmann *et al.*, 2014), are confined or immobilized temporarily in noncontiguous nanometer-scale PM domains (Eggeling *et al.*, 2009; Sahl *et al.*, 2010; Honigmann *et al.*, 2014). In particular, Sahl *et al.* (2010) proposed that, in the PtK2 cell line, a typical nonraft phospholipid (Sezgin *et al.*, 2012) exhibited alternating periods of simple-Brownian diffusion with a diffusion coefficient of ~0.4 μm^2/s, lasting for 7 ms on average, and temporary immobilization within 6- to 20-nm-diameter domains for 3 ms on average. These results raised the possibility that the picket and fence effects we proposed are not operative in the PtK2-cell PMs, and thus the fence-and-pickets model might be applicable only to a small set of cells. Therefore it was necessary for us to reexamine the PM of the PtK2 cells closely and extensively. Whereas Andrade *et al.* (2015) revisited this issue recently and found that phospholipids are confined by the actin–MSK network, further extensive studies using single-molecule tracking, as used in the studies of many other cells PMs, are necessary.

Therefore the second objective of the present investigation was to examine thoroughly the PM of PtK2 cells in terms of 1) the actin-induced hop diffusion of both phospholipids and TfR, 2) the relationship between the dynamics of membrane molecules and the actin-based MSK structure, and 3) a comparison between the fence effect and the picket effect. By accomplishing the first and second objectives of the present research, we aimed at establishing the generality of the fence-and-pickets model.

The third objective of this research was to examine the model of slowed simple-Brownian diffusion for both phospholipids and TfR in cell types in which lipids undergo slow, simple-Brownian diffusion rather than hop diffusion (Schmidt and Nichols, 2004; Lenne *et al.*, 2006; Eggeling *et al.*, 2009; Manzo *et al.*, 2011; Vicidomini *et al.*, 2011; Billaudeau *et al.*, 2013; also see the series of articles by Vrljic *et al.*, 2002, 2005; Nishimura *et al.*, 2006; and Umemura *et al.* 2008), perhaps due to the crowding of TM proteins in the PM rather than

partitioning (Gambin *et al.*, 2006; Frick *et al.*, 2007), using fluorescence recovery after photobleaching (FRAP) and advanced FCS. Schmidt and Nichols (2004); Lenne *et al.* (2006), and Frick *et al.* (2007) concluded that the actin-based MSK might be involved in slowing the diffusion of TM proteins, but not phospholipids, in the PM. Thus various models for the mechanisms controlling phospholipid dynamics in the PM have been proposed, which warrants further study of the regulation mechanisms for phospholipid diffusion in the PM.

In the present research, we are particularly concerned with three models of molecular dynamics in the PM and PM domain structure: models involving 1) temporary binding and/or transient entrapment within nanoscale domains (Eggeling *et al.*, 2009; Sahl *et al.*, 2010; Honigmann *et al.*, 2014), 2) slow, simple-Brownian diffusion (Gambin *et al.*, 2006; Frick *et al.*, 2007), and 3) pickets and fences.

For clearer presentation of the data, we focus here on results obtained in the PM of PtK2 cells (except for relevant results with Cy3-TfR and Cy3-DOPE). When comparison with results in other cell types is needed (to establish their generality), we indicate their use (see later discussions of Figures 4B, 5G, and 7B). Additional results in other cell types are shown for comparison in Supplemental Figures S1, S4, and S5.

RESULTS

Almost all of the mobile TfR molecules are located in the bulk membrane outside of clathrin-coated pits

All microscopy experiments reported in this article were performed at 37°C. First, TfR was tagged with transferrin conjugated with either Cy3 or Alexa 633. The movement of TfR (a single-path TM protein forming a native covalently-linked dimer) outside and inside the clathrin-coated pits (CCPs) in the PM of T24 cells was observed by single-fluorescent-molecule tracking (SFMT), using a home-built objective lens–type total internal reflection fluorescence (TIRF) microscope operated at video rate (30 Hz, i.e., a time resolution of 33 ms; Iino *et al.*, 2001; Koyama-Honda *et al.*, 2005; Mashanov and Molloy, 2007; Figure 1Ba). The number density of CCPs marked by green fluorescent protein (GFP)–conjugated AP-2α or monomeric red fluorescent protein–conjugated clathrin light chain at low levels was 0.42 ± 0.15 (mean ± SD; 16 images) or 0.58 ± 0.21 (19 images) CCPs/μm^2, respectively (Supplemental Figure S1A, top and middle). The CCP number density determined by electron microscopy was 0.67 ± 0.38 CCPs/μm^2 (19 images). However, since the optical spatial resolution is ~250 nm, the number density obtained by electron microscopy was recounted for fluorescence detection: when the CCPs located within 250 nm were counted as one CCP, the CCP number density became 0.48 ± 0.21 CCPs/μm^2 (Supplemental Figure S1A, bottom), indicating that virtually all CCPs can be visualized by TIRF observations with single-molecule sensitivity.

Single molecules of TfR labeled with Alexa 633–Tf were simultaneously observed with CCPs marked by GFP-conjugated clathrin light chain expressed at low levels (Supplemental Figure S1B; Gaidarov *et al.*, 1999; Ehrlich *et al.*, 2004; Loerke *et al.*, 2009; Taylor *et al.*, 2011; Cocucci *et al.*, 2012). TfR exhibited a mobile time fraction of 89 ± 3.3% (mean ± SD) and an immobile time fraction of 11 ± 3.3%, of which 81 ± 6.6% occurred in the CCPs (colocalization of TfR with CCPs and temporary immobilization were detected as described by Koyama-Honda *et al.* (2005) and Shibata *et al.* (2012), respectively; total observation time was 314 s; total number of immobilization events was 28; five independent experiments). These results indicate that virtually all of the mobile TfR molecules are located outside the CCPs. In this study, since we were interested in the translational diffusion of TfR outside CCPs,

we selected trajectories >100 frames (3.3 s) that do not exhibit temporary immobilization.

TfR exhibits effective simple-Brownian diffusion in SFMT at a slow rate (video rate) in five mammalian cell lines

Single-molecule images and trajectories of TfR tagged with Cy3-Tf (Cy3-TfR) in the apical PM of epithelial PtK2 cells were obtained with the same TIRF microscope at a slow rate (video rate) but with oblique-angle illumination (Figures 1Ca and 2A, top left), and each single-molecule trajectory was classified into the 1) simple-Brownian, 2) directed, or 3) suppressed diffusion mode in the following manner (Kusumi *et al.*, 1993; Hiramoto-Yamaki *et al.*, 2014).

First, we obtained the plot of the mean-squared displacement (MSD) against the time interval (Δt), called the single-molecule MSD–Δt plot, for each trajectory.

Second, we calculated the parameter RD(N, n) = MSD($n\delta t$)/$4D_{1–3}n\delta t$ for each trajectory, where n is the number of steps used for the analysis in the trajectory of N steps ($1 \leq n \leq N$), δt is the camera frame time (thus the actual time for n steps is $n\delta t$; Figure 2B, right), and $D_{1–3}$ is the initial slope of the MSD–Δt plot divided by 4 (see *Materials and Methods* and Figure 2B; as a macroscopic diffusion coefficient obtained from data recorded at video rate, $D_{2–4}$ was used for consistency with the previous results). Here RD(N, n) describes the long-term (for a period of $n\delta t$) relative deviation of MSD($n\delta t$) from the simple-Brownian model (see *Materials and Methods*). Because $n\delta t$ (Figure 2B, right) is the key time scale used for evaluating the deviation from the ideal simple-Brownian diffusion mode, in this article, RD(N, n) will be expressed in the form of RD(n, $n\delta t$) to clearly indicate the time scale of the classification of each trajectory (see the *x*-axes of Figures 2, B right, and C, and 3B). The average value of RD(N, n) (or RD(n, $n\delta t$)) for the ensemble of molecules undergoing simple-Brownian diffusion will be 1, whereas those for the ensemble of molecules undergoing directed or suppressed diffusion will be >1 or <1, respectively. However, note that the RD(N, n) value *for each individual trajectory* would vary greatly from trajectory to trajectory.

Third, we obtained the RD(N, n) distribution for simple-Brownian particles by generating 5000 simple-Brownian trajectories, using the Monte Carlo simulation (Figure 2C, top). On the basis of this distribution, we obtained the RD(N, n) values giving the 2.5th percentiles of the particles from both ends of the distribution, referred to as RD$_{min}$ and RD$_{MAX}$, respectively (shown in Figure 2C by vertical red and cyan lines, respectively).

Fourth, we classified each experimental single-molecule trajectory in the following manner. When its RD(N, n) value was <RD$_{min}$ or >RD$_{MAX}$, it was classified into the suppressed- or directed-diffusion mode, respectively, and otherwise it was classed into the simple-Brownian diffusion mode. Note that this classification is based strictly on the statistical deviations from simple-Brownian diffusion, and no diffusion model is assumed. To emphasize this point, we use the term "suppressed diffusion" here rather than the term "confined-hop diffusion" used in previous publications (Kusumi *et al.*, 1993; Fujiwara *et al.*, 2002; Suzuki *et al.*, 2005; Umemura *et al.*, 2008). Previously, since all of the MSD–Δt plots for the trajectories classified into the suppressed diffusion mode could be fitted with the equation describing hop diffusion (Powles *et al.*, 1992), the term "confined-hop diffusion" was used for particles exhibiting the "suppressed diffusion mode."

Note that the average value of RD(N, n) (or RD(n, $n\delta t$)) for the ensemble of molecules undergoing simple-Brownian diffusion will be 1, but its most likely value or the value at which RD peaks is not necessarily 1 (Figure 2C, top). For further explanations of the RD(N,
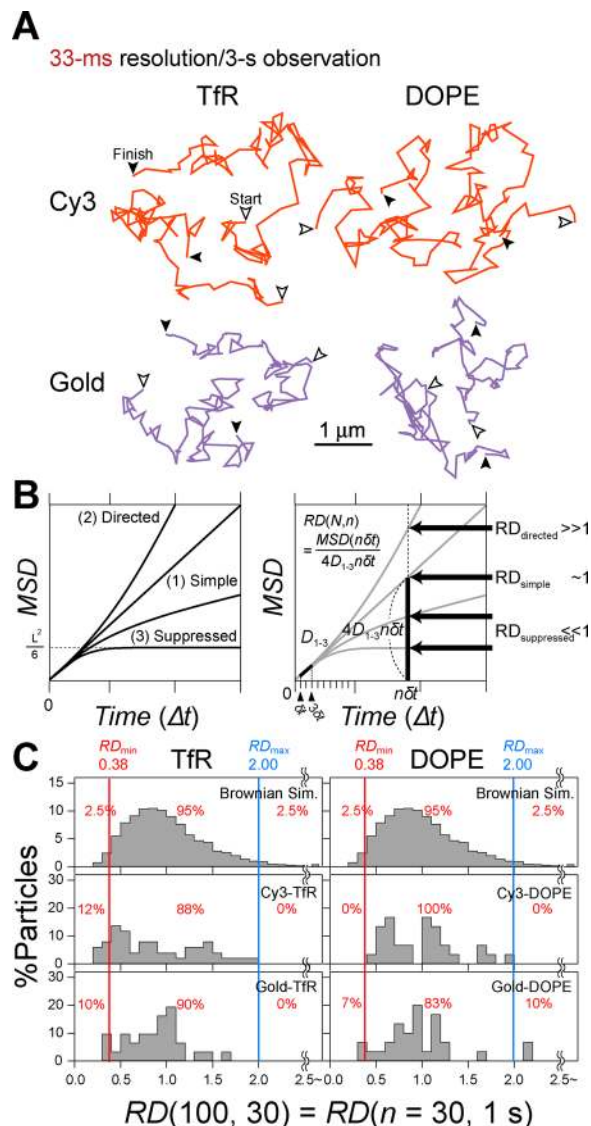

FIGURE 2: Method for classifying the trajectories into simple-Brownian-, suppressed-, and directed-diffusion modes and its application to TfR and DOPE trajectories (with fluorescent and gold probes) obtained in the PtK2-PM at video rate. (A) Representative trajectories of TfR (left) and DOPE (right) tagged with Cy3 (top) or gold (bottom) probes in the PtK2-PM. (B) Left, theoretical MSD–Δt curves for 1) simple-Brownian, 2) directed, and 3) suppressed diffusion (for the same short-term diffusion coefficients = initial slope at time 0). Right, motional mode classification based on RD(N, n). (C) Distribution of RD(N, n) for N = 100 and n = 30 (1 s), used for the classification of the trajectories into different diffusion modes (left, TfR; right, DOPE). Top, simple-Brownian trajectories generated by Monte Carlo simulation (the same graphs are used for both TfR and DOPE). The 2.5th percentiles of the distribution from both ends, RD$_{min}$(100, 30) and RD$_{MAX}$(100, 30), are shown by red and cyan vertical lines, respectively. Middle, SFMT at normal video rate, using Cy3 as a probe. Bottom, SPT at normal video rate, using gold particles as probes.

n) distribution for simple-Brownian particles, see Supplemental Figure S2 and *Materials and Methods*.

About 90% of the Cy3-TfR trajectories in epithelial PtK2 cells observed at video rate were classed as undergoing effective simple-Brownian diffusion, as shown in Figure 2C, left middle. Here the term "effective" is used because, later in this article, we show that the TfR

molecules actually undergo suppressed (more specifically, hop/confined) diffusion, and the simple-Brownian diffusion detected here is only true in the limited time scale >33 ms, representing long-term macroscopic diffusion. Similar observations and analyses for four other cell lines—HEPA-OVA, HeLa, T24, and NRK cells—revealed that TfR mostly undergoes effective simple-Brownian diffusion on the time scale of 33 ms to 1 s (30 video frames) in all of these cell types (Supplemental Table S1). Therefore the diffusion on this time scale can be described by a single effective diffusion coefficient, and here we used $D^{eff}(33\ ms)_{100\ ms}$ (obtained by the linear fitting of the MSD–Δt plot between 67 and 132 ms, with a midpoint of 100 ms, for data obtained at 33-ms time resolution), following Suzuki et al. (2005) and Umemura et al. (2008). The median and mean values of $D^{eff}(33\ ms)_{100\ ms}$ for TfR are summarized in Table 1. All values cited in this article refer to the median values, unless otherwise specified.

The unsaturated phospholipid Cy3-DOPE exhibited effective simple-Brownian diffusion in SFMT at a slow rate (video rate) in five mammalian cell lines

We next examined the movement of single molecules of the typical nonraft phospholipid DOPE tagged with Cy3 in the head group region (Cy3-DOPE). The majority of their trajectories (Figures 1, Bb and Cb, and 2A, top right; observed in the PM of PtK2 cells) were statistically classified into the simple-Brownian diffusion mode (Figure 2C, right, middle) in all five mammalian cell lines (Supplemental Table S1). Their median $D^{eff}(33\ ms)_{100\ ms}$ values are summarized in Table 1.

Single-molecule observations with enhanced time resolution revealed that virtually all TfR and DOPE molecules undergo suppressed diffusion

Next we used a 40-nm-diameter colloidal gold particle as a probe (Figure 1, B and C, c and d), which enabled observations up to a frame rate of 40,500 frames/s (every 0.025 ms; Figure 3A). The colloidal gold labeling was optimized as described previously (see Materials and Methods).

At video rate, >80% of the trajectories of gold-tagged TfR and DOPE (gold-TfR and gold-DOPE, respectively) in the PtK2-cell PM were classified into the simple-Brownian mode (Figure 3B and Supplemental Figure S3). With an increase of the frame rate, more trajectories were classified into the suppressed-diffusion mode, and at 40,500 Hz, practically all of the gold-TfR and DOPE trajectories were classified into the suppressed-diffusion mode (Figure 3B and Supplemental Figure S3; see the enlarged trajectories in Figure 3A).

These results indicated that the suppressed movement, detectable at 0.025-ms resolution, was hidden at the slower observation rates. This is why we used the term "effective" simple-Brownian diffusion for the results obtained at slower camera frame rates (i.e., at lower time resolutions).

TfR and DOPE underwent hop diffusion and exhibited the same compartment size in the five examined cell types

The enlarged 0.025-ms-resolution trajectories of gold-TfR and DOPE recorded in the PtK2-cell PM are shown at the bottom of Figure 3A. These trajectories, as well as others obtained at 0.025-ms resolution and classified into the suppressed-diffusion mode, were analyzed by a computer program developed to detect the occurrence of hops between the two compartments (Fujiwara et al., 2002; Suzuki et al., 2005). The detected plausible hop events define plausible compartments, which are shown in various colors in the enlarged trajectories at the bottom of Figure 3A. Such hop events were detected in virtually all of the trajectories classified into the suppressed-diffusion mode, whereas in the computer-generated

simple-Brownian trajectories, hop events were detected in only 4% of the trajectories, suggesting that suppressed diffusion is induced by the temporary confinement plus hop movements (hop diffusion).

Next we fitted the ensemble-averaged MSD–Δt plots for gold-TfR and gold-DOPE by an in-house program, based on the equation representing the model of idealized hop diffusion (Powles et al., 1992), in which a particle undergoes diffusion with the true (microscopic) diffusion coefficient between the barriers, D_{micro}, in the presence of semipermeable barriers placed at an equal distance (L), thus providing the macroscopic (long-term) diffusion coefficient over many compartments, D_{MACRO} (hop-diffusion fitting; Figure 4A; Powles et al., 1992; Fujiwara et al., 2002; Murase et al., 2004; Suzuki et al., 2005). The fits were good for both gold-TfR and DOPE, supporting the hop-diffusion model.

The MSD–Δt plot for each trajectory (single-molecule MSD–Δt plot) was then fitted by the hop-diffusion fitting, providing the compartment size L averaged over a single trajectory. The distribution of L over all of the molecules is shown in Figure 4B (top). Of importance, the compartment size distributions for a TM protein, TfR, and a phospholipid, DOPE, were similar to each other, with median values of 43 and 46 nm, respectively (Figure 4B, top, and Table 1). This agreement was found in all five cell types examined here (Figure 4B and Table 1), suggesting that the underlying mechanisms for confining TM proteins and phospholipids are the same, that is, MSK-meshwork-induced compartments.

One might be concerned that gold-TfR, including even mobile particles, might be extensively entrapped in CCPs and undergo slow hop diffusion there, even though most of the mobile Cy3-TfR is likely to be located outside the CCPs (Supplemental Figure S1). We believe that the influence of gold-TfR entrapped in CCPs on the compartment size reported here was quite small, for the following reasons:

1. In the histograms shown in Figure 2C, left, comparison of the histogram for Cy3-TfR (middle) and that for gold-TfR (bottom) shows that at 33-ms resolution, there is no indication that gold-TfR is more trapped in CCPs than Cy3-TfR, excluding the long-term trapping of gold-TfR in CCPs.

2. The CCP architecture is considered to be basically the same in all five of the cell lines used here, but we did not detect any features common to all of them in the compartment–size histograms for TfR shown here.

3. Furthermore, in the same histograms, we failed to detect any differences in the compartment size distributions between gold-TfR and gold-DOPE.

Estimation of the average residency time within a compartment

We estimated residency times (τ's) of TfR and DOPE within a compartment from the median L values determined for gold-labeled molecules, using high-speed single-particle tracking (SPT) and $D_{MACRO} = D^{eff}(33\ ms)_{100\ ms}$ measured with Cy3 probes using SFMT, based on the equation $\tau = L^2/[4D^{eff}(33\ ms)_{100\ ms}]$ (Table 1). As described in Murase et al. (2004) and Suzuki et al. (2005), $D_{MACRO} = D^{eff}(33\ ms)_{100\ ms}$ has to be used for this calculation for the following reason. Each membrane molecule exhibits two diffusion coefficients: 1) the short-term diffusion coefficient, obtained on the time scale of 75 µs (25 µs × 3), representing the diffusion coefficient within a compartment (D_{micro}), and 2) the long-term diffusion coefficient, obtained on the time scale longer than the residency time within a compartment, representing the diffusion coefficient in space scales several times longer than the

Cell	Molecule	SPT Percentage hop	L (nm)	Time resolution (ms)	Observation period* (ms)	N[†]	SFMT $D^{eff}(33\ ms)_{100\ ms}$ (µm²/s)	N[†]	Calculated τ (ms)
PtK2	TfR	100	43 (45 ± 1.9)	0.025	1.5	54	0.48 (0.53 ± 0.037)	51	0.96
	DOPE	100	46[‡] (49 ± 2.7)[‡]	0.025	1.5	50	0.48 (0.53 ± 0.055)	30[d]	1.1
HEPA-OVA	TfR	100	45 (46 ± 2.5)	0.025	3.7	32	0.18 (0.21 ± 0.017)	34	2.8
	DOPE	100	48[‡] (46 ± 2.3)[‡]	0.025	3.7	28	0.21 (0.37 ± 0.032)	191[d]	2.7
HeLa	TfR	97	64 (72 ± 4.9)	0.025	3.7	59	0.15 (0.16 ± 0.0091)	46	6.8
	DOPE	100	68 (68 ± 3.2)	0.025	3.7	84[a]	0.17[§] (0.19 ± 0.019)[§]	29	6.8
T24	TfR	97	100 (120 ± 10)	0.11	120	38	0.17 (0.19 ± 0.0081)	174	15
	DOPE	100	110 (120 ± 9.7)	0.025	6.7	35[a]	0.34[‖] (0.35 ± 0.019)[‖]	60	8.9
NRK (smaller compartment)	TfR	91	260 (270 ± 10)	0.025	72	107[b]	0.29 (0.29 ± 0.011)	61	58
	DOPE	85	230 (240 ± 11)	0.025	30	90[b]	1.1[¶] (1.2 ± 0.071)[¶]	90[e]	13
NRK (larger compartment)	TfR	84	710 (720 ± 55)	33	3000	70[b]	0.24[#] (0.30 ± 0.026)[#]	61	530
	DOPE	92	750 (800 ± 29)	2	3000	84[b]	0.34[#] (0.42 ± 0.025)[#]	27[f]	410
NRK (blebbed PM)	TfR	26	NA[@]	0.025	10	19	8.1[∞] (8.0 ± 0.71)[∞]	ND[g]	NA[@]
	DOPE	13	NA[@]	0.025	10	30[c]	8.5[∞] (8.9 ± 0.47)[∞]	ND[g,h]	NA[@]

Median values, as well as mean ± SE values (in parentheses) are given for the compartment size and $D^{eff}(33\ ms)_{100\ ms}$.

*The time period in the MSD–Δt plot used for "hop fitting."

[†]Number of examined molecules. The notes denoted by symbols and letters describe the relationships of the results obtained here and those previously reported by us (Fujiwara *et al.*, 2002; Murase *et al.*, 2004). They are quite complicated and so are summarized in Supplemental Notes to Table 1.

[¶]$D^{eff}(25\ µs)_{30\ ms}$ obtained with gold-DOPE. The NRK-cell PM has nested 750- and 230-nm compartments (Fujiwara *et al.*, 2002). Therefore it was difficult to determine the diffusion coefficient of DOPE among the 230-nm compartments without the influence of the presence of the 750-nm compartments. It turned out that $D^{eff}_{30\ ms}$ ($D_{50\ ms}$ according to the definition of Murase *et al.*, 2004) better represents the macroscopic diffusion rate of DOPE molecules over 230-nm compartments than $D^{eff}_{100\ ms}$ used for other cells to describe D_{MACRO} in the present study because the latter is strongly affected by the presence of the larger, 750-nm compartments. However, it was impossible to determine $D^{eff}_{30\ ms}$ for Cy3-DOPE due to the insufficient time resolution (33 ms) of SFMT; therefore $D^{eff}(25\ µs)_{30ms}$ obtained with high-speed SPT is shown here (Fujiwara *et al.*, 2002; Murase *et al.*, 2004).

[#]As described in the preceding note, the NRK-cell PM has nested 750- and 230-nm compartments (Fujiwara *et al.*, 2002). Because the residency times of TfR and DOPE molecules in the larger compartments of the NRK cell are much longer than 100 ms, $D^{eff}(33\ ms)_{1.5s}$ (D_{3s} according to the notation by Murase *et al.*, 2004) was used as D_{MACRO}, which described the diffusion coefficient among the larger compartments.

[@]Not applicable because the trajectories classified into the simple-Brownian mode should not exhibit compartmentalization and L cannot be determined, and those classified into the hop-diffusion mode exhibited compartment sizes with extreme variations; also not applicable for τ because L could not be defined.

[∞]$D^{eff}(25\ µs)_{75\ µs}$ obtained with gold-TfR (present research) or gold-DOPE (Murase *et al.*, 2004). $D^{eff}(25\ µs)_{75\ µs}$ values for gold-labeled TfR and DOPE are shown in the $D^{eff}(33ms)_{100ms}$ column for SFMT (see note h in the N column). The blebbed PM is round, and single-molecule tracking can only be performed using the very small, quasiflat area on top of the rounded PM. Furthermore, in the blebbed PM, both TfR and DOPE diffuse rapidly and thus move out of the top quasiflat area very quickly. Therefore their diffusion coefficients could be measured using single-molecule tracking only at high frequency (which allows sufficient observations of single particles/molecules during the time the molecules stay in the small top flat area). Namely, SFMT at video rate was useless for obtaining diffusion coefficients of TfR and DOPE in the blebbed PM. Therefore we evaluated the diffusion coefficients of TfR and DOPE in the blebbed PM, using high-speed (25-µs resolution) SPT of gold-TfR and gold-DOPE. Cy3-TfR and Cy3-DOPE might diffuse faster, but the difference would be small because the values obtained here with gold probes are comparable to those from the FRAP data (using fluorescent probes) in artificial lipid bilayer membranes (Kusumi *et al.*, 2012).

TABLE 1: Compartment size L obtained by SPT, $D^{eff}(33ms)_{100\ ms}$ evaluated by SFMT, and residency time within each compartment (τ) calculated from L (SPT, median value) and $D^{eff}(33\ ms)_{100\ ms}$ (SFMT, median value) using the equation $\tau = L^2/4D_{MACRO}$ for TfR and DOPE in PtK2, HEPA-OVA, HeLa, T24, and NRK cells.
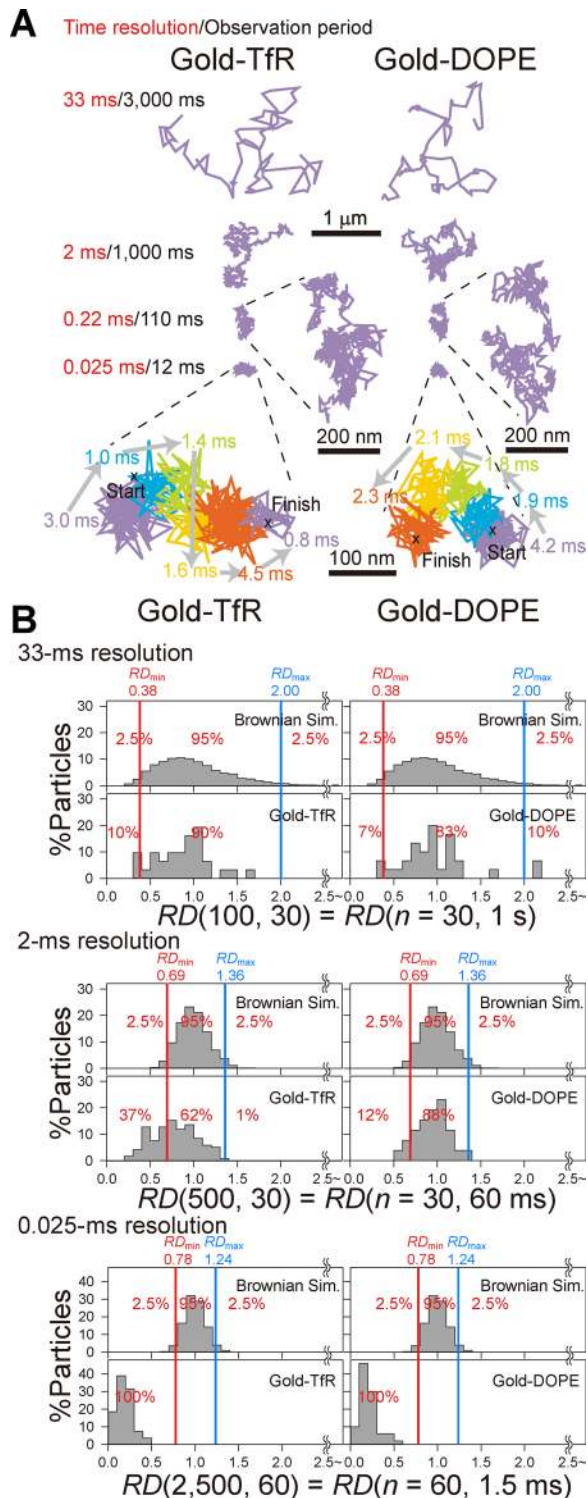
FIGURE 3: Hop diffusion becomes visible only with enhanced frame rates (improved time resolution). (A) Representative trajectories of gold-TfR (left) and DOPE (right) in the PtK2-cell PM obtained at systematically varied frame times of 33, 2, 0.22, and 0.025 ms. The trajectories obtained at 0.22- and 0.025-ms resolution are enlarged (see scales). Color coding in the 0.025-ms-resolution trajectories represents plausible compartments detected by a computer program (Fujiwara et al., 2002). The residency time within each compartment is shown. The overlaps of trajectories in adjacent compartments occur due to noise (limited single-molecule localization precision of 19.3 nm for both the horizontal and vertical directions of the camera at

compartment size. Namely, it is the long-term diffusion coefficient that directly reflects the hop frequency or the residency time within a compartment.

We used this method because the direct determination of the residency time within a compartment, using high-speed SPT using colloidal gold probes, is difficult due to gold probe–induced cross-linking of TfR and DOPE (Murase *et al.*, 2004) and also because the hop events occurring on a millisecond time scale could not be observed by the SFMT of fluorescent probes (no cross-linking) due to the insufficient signal-to-noise ratio. Note that the microscopic diffusion of molecules within a compartment is hardly affected by gold-tagging (D_{micro} of gold-DOPE within a compartment was found to be ~8 μm^2/s by Murase *et al.* (2004), which is comparable to the diffusion coefficients of fluorescent lipid molecules in various artificial lipid membranes (Kusumi *et al.*, 2012); the virtual lack of the effect of cross-linking on D_{micro} is consistent with the classical theory of two-dimensional diffusion published by Saffman and Delbrück (1975), which showed that an increase of the diffusant size only very weakly affects the two-dimensional diffusion coefficient). The residency times of TfR and DOPE were in the range of 1–58 and 1–13 ms, respectively, for all five cell types (Figure 4B and Table 1).

The MSK mesh sizes determined by electron tomography agree well with the phospholipid hop-diffusion compartment sizes

The top PMs (apical PMs) of the PtK2 cells were gently removed from the rest of the cells and rapidly frozen from the PM cytoplasmic surface. After deep etching followed by platinum shadowing from the same side, the specimens were observed by electron tomography, as described previously (Morone *et al.*, 2006). In Figure 5, A (right four images) and B (second to fourth images), the boxed areas in the leftmost images were expanded, and the tomography sections obtained every 2.2 nm (superposition of two 1.1-nm-thick slices; 320 × 320 nm) are displayed between 0 and 15.4 nm from the PM cytoplasmic surface. Using these sections, we determined the filaments located within 8.8 nm from the PM cytoplasmic surface (Morone *et al.*, 2006; see *Materials and Methods* for more details), as shown in green in Figure 5C (images for a larger area are shown in Figure 5, D and E). Based on the actin filament diameter (~7 nm) and the platinum particle size (~2 nm), these filaments are

0.025-ms resolution; see *Materials and Methods*). (B) Distributions of RD(n steps, $n\delta t$) (δt = time resolution) for gold-TfR and DOPE in the PtK2-cell PM. For the data obtained at time resolution of 33, 2, and 0.025 ms, the values of the (N, n) pair used here were (100, 30), (500, 30), and (2500, 60), respectively, in terms of the number of steps and (3.3 s, 1 s), (2 s, 60 ms), and (62.5 ms, 1.5 ms), respectively, in terms of time. The (N, n) pair of (100, 30) for the 33-ms resolution data was used, for consistency with the data for Cy3-TfR and Cy3-DOPE (Figure 2C). For the analysis of the data obtained at 2- and 0.025-ms resolution, n values were selected so that the analysis time scale of $n\delta t$ would be useful to detect the non–simple-Brownian nature of the trajectories (Murase *et al.*, 2004). The shapes of the RD distributions for simulated simple-Brownian particles at different time resolutions shown here seem to be quite different because we used the same x-axis scale for all of the RD distributions obtained at different time resolutions, whereas the ratios n/N, which strongly affect the appearance of the RD histograms, used here were quite different for the data obtained on different time scales. To show the shapes of the RD distributions obtained at different time resolutions more clearly, histograms with different x-scales for the same data sets are shown in Supplemental Figure S3.
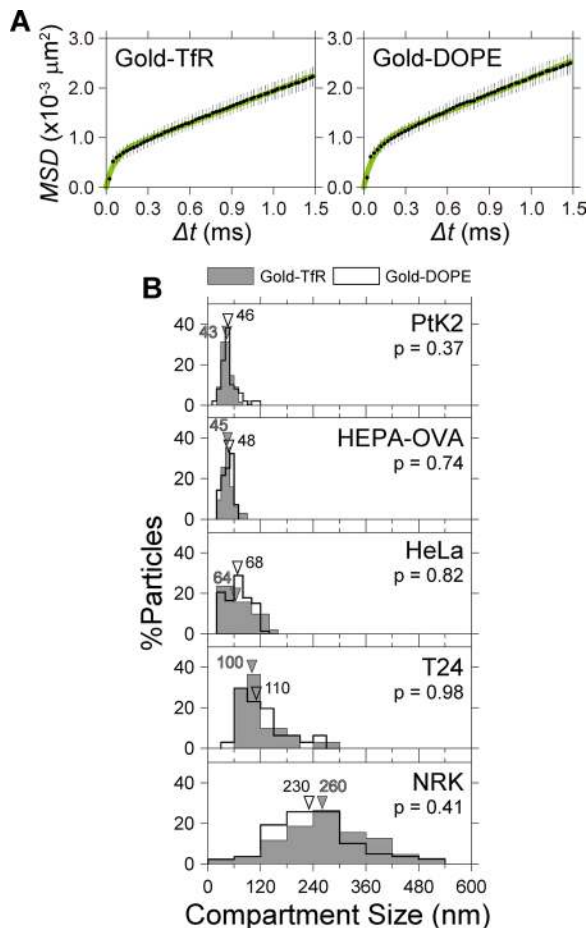
FIGURE 4: The hop-diffusion fitting of the ensemble-averaged MSD–Δt curves obtained at 0.025-ms resolution supports the proposal that suppressed diffusion is actually induced by hop diffusion (A), and the compartment sizes detected by TfR and DOPE are virtually the same for the five cell lines examined here (B). (A) Ensemble-averaged MSD–Δt plots for gold-TfR (left; $n = 54$) and gold-DOPE (right; $n = 50$) obtained at 0.025-ms resolution, with the best-fit curves (green) based on the hop diffusion model (Powles *et al.*, 1992). The error bars represent standard errors. (B) Distributions of the compartment size L for the five different cell lines. Gray bars, TfR (30–101 particles examined for each cell line). Open bars, DOPE (30–77 particles). Arrowheads indicate median values. The difference between TfR and DOPE for each cell line was insignificant (Mann–Whitney U test). The NRK-cell PM is unique, in that it exhibited nested double compartments (Fujiwara *et al.*, 2002; Suzuki *et al.*, 2005). However, we only discuss the smaller compartments in this article. The relationships of the compartment size distributions for gold-DOPE diffusion shown here and those previously reported by us (Fujiwara *et al.*, 2002; Murase *et al.*, 2004) are described in the Supplemental Notes to Figure 4B.

considered to be the actin filaments that formed the MSK fences (Morone *et al.*, 2006).

The areas surrounded by these filaments are colored green in the 0- to 8.8-nm section shown in Figure 5F. The sizes of these green areas were measured, and the distribution of the square root of the area size (the side length, assuming a square shape for the area) for PtK2 cells (blue open bars) is shown in Figure 5G. The distribution for the NRK-cell PM obtained previously (Morone *et al.*, 2006) is shown for comparison (red open bars). The median values are 40 and 200 nm, respectively.

The compartment size distributions obtained from the DOPE diffusion data (closed bars in Figure 5G) exhibited good agreement with the MSK mesh size distributions determined by electron tomography for both PtK2 and NRK cells (and the sizes were very different between these two cell types). This result strongly supports the fence-and-pickets model.

The actin-based MSK architecture in PtK2 cells appeared slightly different from that in NRK cells. The filaments located within 8.8 nm from the PM cytoplasmic surface, which were considered to be bound to the PM cytoplasmic surface, were quite often accompanied by (aligned with) another actin filament that was not bound to the PM cytoplasmic surface (Figure 5, A–E). How this influences the fence and picket effects is unknown. An attempt was made to perform electron tomography experiments after the treatment with an actin-modifying drug, latrunculin A. For the electron tomography work, the apical PM, which we always observed for single-particle (fluorescent molecule) tracking of membrane molecules here, was cleaved off for the observation. For this, we first attached small coverslips to the apical PM and gently removed them so that the apical PM came off with the coverslips. However, after latrunculin A treatment, by unknown reasons, the coverslips did not attach the apical PM well, and so when the coverslips were removed and inspected, we could hardly find any PM there.

Effects of actin-modifying drugs

We examined and compared effects of actin-modulating drugs on the diffusion of gold-TfR and gold-DOPE using high-speed SPT at a time resolution of 0.025 ms. In all of the drug treatment experiments, the drugs were added while the cells were being observed under the microscope and maintained at 37°C, and high-speed SPT was performed between 5 and 30 min after drug addition. Note that the conditions for drug treatment (concentrations and durations) were adjusted so that the drug treatment did not cause the overall cell shape changes.

In the PM of PtK2 cells, we did not detect any statistically significant effects of latrunculin A on the compartment size sensed by TfR even at higher concentrations (6 and 54 μM for 5–30 min at 37°C) (Figure 6A, left top and middle, and Table 2). Following the observations by Murase *et al.* (2004), who found that cytochalasin D, but not latrunculin A, effectively modulated the actin MSK and DOPE diffusion in FRSK cells, we examined the effect of cytochalasin D on the PtK2-cell PM. After the addition of 5 μM cytochalasin D (Figure 6A, left, bottom, and Table 2), the compartments became largest during the first 5–10 min and regained their original sizes during the following 10–15 min (Figure 6A, right with yellow background, and Table 2), indicating that PtK2 cells react readily to the cytochalasin D treatment but recover quickly, consistent with previous findings (Hiramoto-Yamaki *et al.*, 2014). The controversies over the effects of actin modulation (Vrljic *et al.*, 2002, 2005; Schmidt and Nichols 2004; Lenne *et al.*, 2006; Nishimura *et al.*, 2006; Frick *et al.*, 2007) might be due to the complex counterreactions of the cells responding to the actin-modulating drugs.

We determined the compartment size for gold-DOPE under the conditions in which the compartment size for gold-TfR became the largest, that is, between 5 and 10 min after the addition of 5 μM cytochalasin D (Figure 6B, bottom, and Table 2). Under these conditions, the compartment size for Gold-DOPE was also increased, and the sizes for gold-TfR and gold-DOPE were virtually the same (no statistically significant difference). This result further indicates that the compartment sizes for TfR and DOPE are determined by a similar mechanism, that is, the actin-based MSK. Of interest, the residency times of TfR and DOPE within a compartment both increased
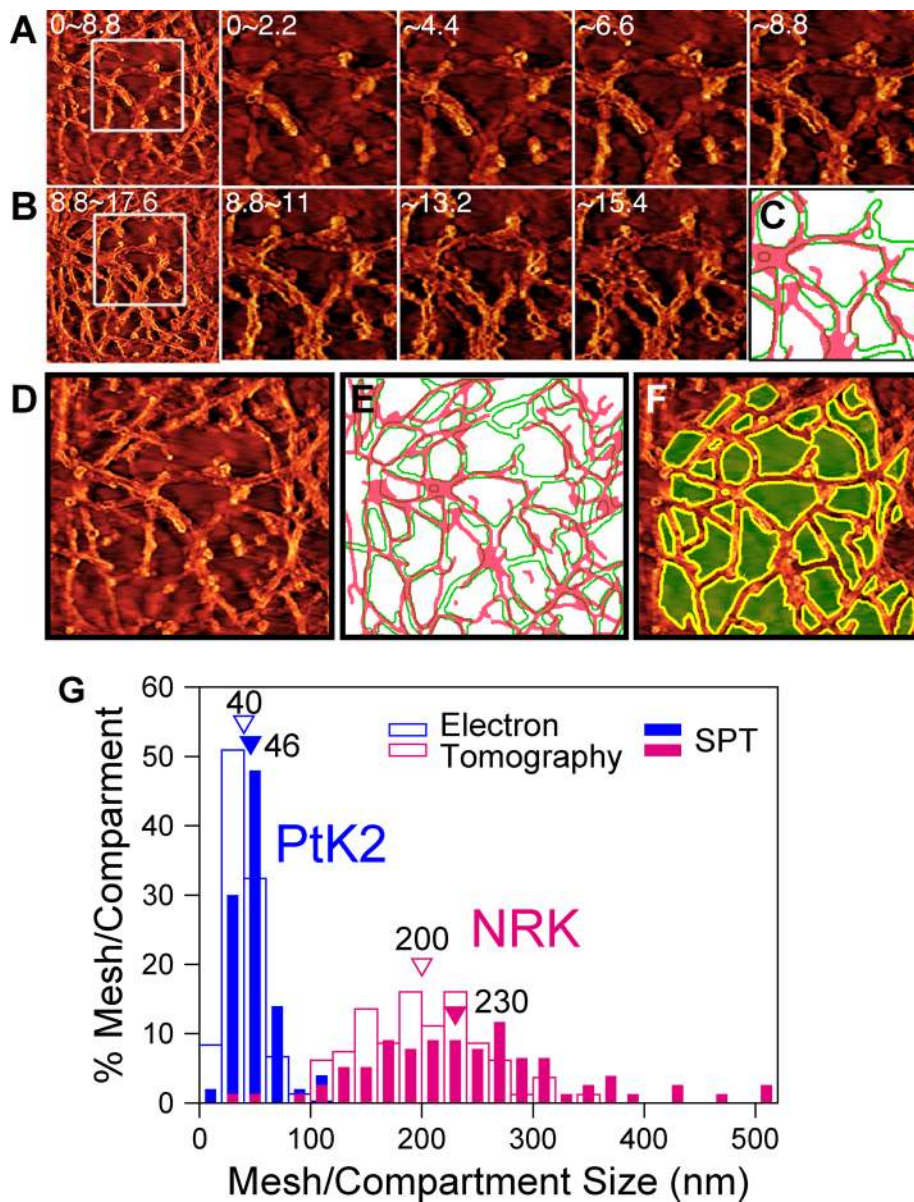
FIGURE 5: The sizes of the MSK meshwork on the PM cytoplasmic surface determined by electron tomography agree well with the compartment sizes determined from the gold-DOPE diffusion measurements. (A, B) Electron tomography images of the PM cytoplasmic surface of the PtK2 cell. The images on the far left are the 0- to 8.8-nm and 8.8- to 17.6-nm sections, each comprising a stack of eight 1.1-nm sections of 640 × 640 nm. These are from a series of 133 image sections (1.1 nm thick) from the cytoplasmic surface after the tilt and the long-wavelength undulation of the cell surface were corrected. The areas enclosed by the white squares in these images (320 × 320 nm) are expanded on the right, with a section thickness of 2.2 nm (two 1.1-nm sections are superimposed). (C) The outline of each actin filament adjacent to the PM cytoplasmic surface (green, observed in the section of 0–2.2 nm and fading out in the sections of 8.8–11.0 and 11.0–13.2 nm) and the outline of each actin filament that could not be observed in the first and/or second sections (0–2.2, 0–4.4, and 2.2–4.4 nm) from the membrane surface and that does not fade out even in the section of 13.2–15.4 nm from the surface (red), as determined from the sections in A and B (320 × 320 nm). (D) The image of the 0- to 8.8-nm section, that is, the image expanded from the leftmost image in A (640 × 640 nm). (E) The outline of actin filaments in a greater view field (640 × 640 nm). (F) Superimposition of image (D) and the green outline (E). The first-layer actin filaments are outlined in yellow, and the areas surrounded by these actin filaments are green. (G) Comparison of the distributions of the actin-MSK mesh size from electron tomography (green areas in F; open bars) with those of the compartment sizes determined from the gold-DOPE diffusion data (closed bars) for PtK2 (blue) and NRK (magenta; from Morone et al., 2006) cells.

(Table 2), perhaps due to the increased compartment sizes (reduced frequencies of arriving at the compartment boundaries).

The mechanisms for the actions of latrunculin A (stabilizing G actin) and cytochalasin D (blocking the fast-polymerizing end) on the actin filament are quite different, and perhaps, as a result, their actions strongly depend on the cell type. We previously found that one works but not the other (to induce changes in the hop diffusion properties) in different cell types; for instance, in FRSK cells, cytochalasin D, but not latrunculin A, modified the actin-based MSK (Murase et al., 2004), but the situation was just the opposite in CHO cells (Umemura et al., 2008). The reason for such variations will be difficult to clarify, but they probably reflect the subtler differences in the organizations and interactions of the actin-based MSK.

Similar experiments studying the effect of actin modulation on the hop diffusion of gold-DOPE and TfR using NRK cells gave very similar results (Supplemental Figure S4 and Supplemental Table S2).

Diffusion in the PM blebs

Ultrafast SPT of gold-Tf at 0.025-ms resolution was performed in the actin-depleted PM, which was formed by PM blebbing and further latrunculin A treatment (see *Materials and Methods*). Previously, the diffusion of gold-DOPE was examined in the blebbed PM, but the diffusion of TM proteins has never been examined there. Typical trajectories of gold-DOPE (selected from the set of trajectories obtained for the report by Fujiwara et al., 2002) and gold-TfR (obtained in the present research) are shown in Supplemental Figure S5A (NRK cells; blebbed PMs were difficult to form from the PM of PtK2 cells). Most of the trajectories of both gold-TfR and gold-DOPE were classified into the simple-Brownian diffusion mode (Supplemental Figure S5B), in stark contrast to the observations made in the intact PM, further suggesting that the underlying mechanisms for the hop diffusion of TfR and DOPE are related to the actin-based MSK. The microscopic diffusion coefficients, $D^{eff}(25\ \mu s)_{75\ \mu s}$ (8.1 and 8.5 μm^2/s for gold-Tf and DOPE, respectively; Supplemental Figure S5C), were almost as fast as that of gold-DOPE in large, unilamellar vesicles (~9 μm^2/s; Fujiwara et al., 2002), indicating that the actin-based MSK is predominantly responsible for non-Brownian movements of both TfR and DOPE in intact PMs.

These $D^{eff}(25\ \mu s)_{75\ \mu s}$ values found in the blebbed PMs are consistent with the microscopic diffusion coefficient within a
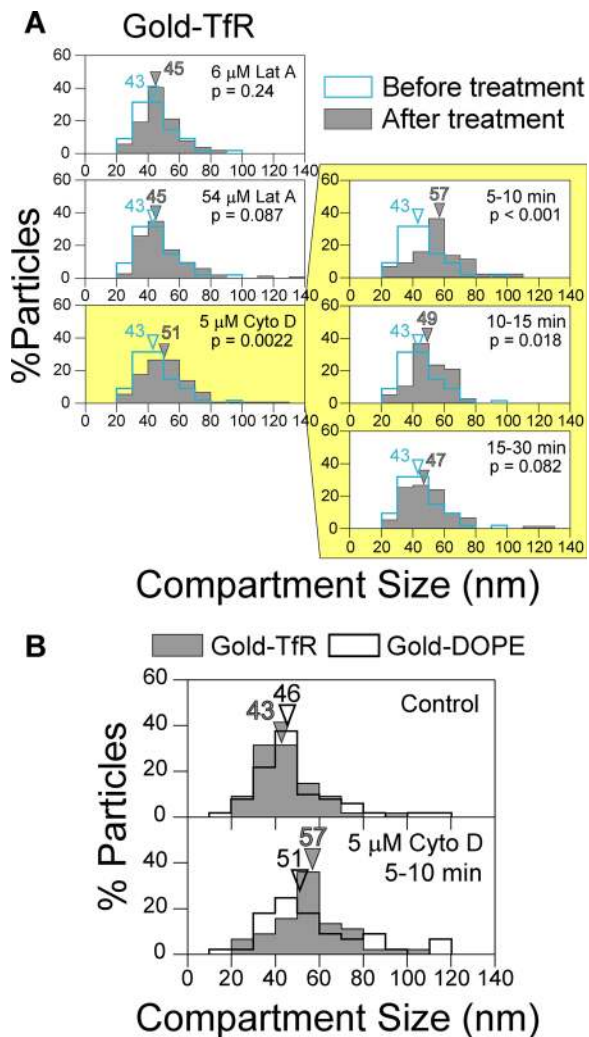
FIGURE 6: Cytochalasin D, but not latrunculin A, increased the PM compartment size in PtK2 cells, and its effect was greatest 5–10 min after its addition to the cells. Under these conditions, the compartment sizes were increased for both gold-TfR and gold-DOPE, but no statistically significant differences were found between these two probes. (A) Effects of latrunculin A and cytochalasin D on the compartment size for gold-TfR in the PtK2-cell PM, showing the dramatic dependence on the drug type and the cytochalasin D treatment duration. p values were determined by the Mann-Whitney U test. The compartment size distribution for gold-TfR in the intact PM of PtK2 cells (blue histograms) is reproduced in all of the boxes for comparison. This histogram is the same as that shown in Figure 4B, top, and is reproduced here for comparison with those after the treatment with actin-modifying drugs. (B) Compartment size distribution for gold-TfR at 5–10 min after the addition of cytochalasin D (reproduced from the top graph in A) compared with that for gold-DOPE. The data in the top graph show the compartment size distributions in intact cells (control) reproduced here from Figure 4B, top, for comparison.

compartment, D_{micro}, determined previously (Fujiwara *et al.*, 2002; Murase *et al.*, 2004). These $D^{eff}(25\ \mu s)_{75\ \mu s}$ values for gold-TfR (8.1 $\mu m^2/s$) and gold-DOPE (8.5 $\mu m^2/s$) were greater than the macroscopic diffusion coefficients, D_{MACRO}, determined for Cy3-TfR and Cy3-DOPE (Table 1; see the data for NRK cells) by factors of 28–34 and 7.7–25, respectively. Owing to the nested double compartmentalization of the NRK-cell PM, the comparison is somewhat difficult,

but the difference between D_{micro} and D_{MACRO} for the smaller compartment, averaged between gold-TfR and gold-DOPE, is about a factor of 17 (this factor is greater if we include the larger compartments). This indicates that all models and theories that attempt to explain the PM domain architecture and the molecular dynamics there must be able to explain the 17-times-slower diffusion in the PM than in the blebbed PM and artificial lipid membranes. Furthermore, they should be able to reproduce the dependence of the diffusion mode on the observation frequency shown in Figure 3.

The extracellular matrix and the extracellular domains of TM proteins are not responsible for the 17-times-slower macroscopic diffusion

Gold-TfR diffusion was examined after a mild trypsin treatment of PtK2 cells under conditions in which 51% of the extracellular domains of membrane proteins plus extracellular cell matrix proteins bound to the cell surface (cell surface–bound biotin probe), 55% of collagen type I, and 61% of chondroitin sulfate were removed (under these conditions, 74% of TfR remained). The $D^{eff}(33\ ms)_{100\ ms}$ value of gold-TfR was not significantly affected (median, 0.31 $\mu m^2/s$, $n = 78$), as compared with that in the intact PM (0.30 $\mu m^2/s$, $n = 31$). Note that this was observed using the 40-nm gold probe, which would interact and collide with the extracellular matrix and the extracellular domains of TM proteins much more extensively than would the Cy3 probe. Therefore the extracellular matrix and the extracellular domains of TM proteins are not likely to be involved in the 17-times-slower diffusion (compared with the diffusion in the blebbed PM) or the hop diffusion of TfR in the PM.

These results are consistent with the previous observations of gold-DOPE after trypsinization in FRSK and NRK cells. Gold-DOPE diffusion after trypsinization under the conditions of removing ~60% of the cell-surface biotin probe and chondroitin sulfate in FRSK cells (Murase *et al.*, 2004) and that after the removal of ~60% of the cell-surface biotin probe and 83% of heparan sulfate glycosaminoglycan in NRK cells (Fujiwara *et al.*, 2002) were examined previously. No effect of the trypsin treatment on gold-DOPE diffusion was found.

Effects of fence versus pickets

First, the size of the TfR cytoplasmic domain was increased from 134 amino acids (aa) to 762 and 1082 aa by the addition of two and three Halo-protein tags (see the first four molecules from the left in the schematic diagram in Figure 7A and its legend), and the movements of the mutated molecules were observed at the level of single molecules (after proper fluorescence labeling) at video rate. The hop diffusion could not be directly observed at this frame rate, but the macroscopic diffusion coefficient, $D^{eff}(33\ ms)_{100\ ms}$, provides a useful yardstick for the hop frequency of the mutated TfRs (because the compartment size should stay the same). In both PtK2 and T24 cells, $D^{eff}(33\ ms)_{100\ ms}$ was slightly but statistically significantly decreased, although the addition of a single Halo-protein (448 aa) did not change the diffusion coefficient (Figure 7B, second to fourth pairs of graphs, and Supplemental Table S3). This result indicates that the cytoplasmic domain is involved in confining TfR within the compartments induced by the actin-based MSK.

Second, two point mutations that jointly block TfR dimer formation were included (C89S and C98S, with a single Halo-tag protein in the cytoplasm for probing, providing the cytoplasmic domain size of 381 aa; fifth molecule in Figure 7A). The $D^{eff}(33\ ms)_{100\ ms}$ value for this monomer molecule was significantly larger than that for the dimer of TfR-Halo chain plus endogenous TfR chain (cytoplasmic domain size, 448 aa; second molecule in Figure 7A) in both PtK2 and

Treatment	Molecule	SPT				SFMT		
		Percentage hop*	L (nm)[†]	P[§]	N[‖]	$D^{eff}(33\ ms)_{100\ ms}$ ($\mu m^2/s$)[¶]	N[‖]	Calculated τ (ms)
Control	TfR	100	43 (45 ± 1.9)[‡,1]		54	0.48 (0.53 ± 0.037)	51	0.96
	DOPE	100	46[#] (49 ± 2.7)[‡,2,#]		50	0.48 (0.53 ± 0.055)	30[a]	1.1
Latrunculin A (6 µM, 5–30 min)	TfR	100	45 (47 ± 1.7)[N1]	0.24	52	0.53 (0.56 ± 0.024)	57	0.96
Latrunculin A (54 µM, 5–30 min)	TfR	100	45 (49 ± 1.3)[N1]	0.087	155	0.58 (0.61 ± 0.024)	54	0.87
Cytochalasin D (5 µM, 5–30 min)	TfR	100	51 (52 ± 1.3)[Y1]	0.0022	157	0.37 (0.40 ± 0.010)	196	1.8
Cytochalasin D (5 µM, 5–10 min)	TfR	100	57 (56 ± 2.5)[Y1]	<0.001	44	0.38 (0.42 ± 0.023)	54	2.1
	DOPE	95	51 (58 ± 3.4)[Y2]	0.023	44	0.40 (0.36 ± 0.020)	33	1.6
Cytochalasin D (5 µM, 10–15 min)	TfR	100	49 (50 ± 1.9)[Y1]	0.018	38	0.38 (0.39 ± 0.022)	32	1.6
Cytochalasin D (5 µM, 15–30 min)	TfR	100	47 (50 ± 2.0)[N1]	0.082	75	0.36 (0.39 ± 0.013)	110	1.5

*Percentages of trajectories classified into the hop-confined diffusion mode, determined for 1.5-ms observation at a 0.025-ms resolution; see Figures 2B and 3B, bottom, and Materials and Methods.

[†]The differences in L between TfR and DOPE are statistically insignificant for control (without actin modulation) and for the cells 5–10 min after the addition of 5 µM cytochalasin D. The median L values, as well as the mean ± SE L values (in brackets), are given.

[‡]Additional superscripts Y and N indicate results of the statistical test. The distributions selected as the basis for the comparison are shown by the double dagger (‡). Different numbers (1 and 2) indicate different bases. The superscript Y or N indicates that the distribution is or is not significantly different from that shown by the double dagger superscript, respectively ($p < 0.05$ or >0.05, respectively). For the statistical test, see the following note.

[§]p values of the Mann–Whitney U test.

[‖]Number of examined molecules. All of the TfR data shown here were obtained in the present research. For the gold-DOPE results, the superscript a in the N column indicates that the $D^{eff}(33\ ms)_{100\ ms}$ value (for Cy3-DOPE in the control PtK2-cell PM) is from Murase et al. (2004).

[¶]The median values, as well as the mean ± SE values (in parentheses), are given.

[#]Although the L values for gold-DOPE in the PtK2-cell were previously published (Murase et al., 2004), to ascertain the accuracy of the data for small compartment sizes, the experiments were redone in the present research, and the newly obtained values are shown here. No statistically significant differences from the previously published values were found.

TABLE 2: Effects of drug-induced actin modulation in PtK2-cell PMs on the compartment size L obtained by SPT (0.025-ms time resolution), $D^{eff}(33\ ms)_{100\ ms}$ evaluated by SFMT, and residency time within each compartment (τ) calculated from L (SPT, median value) and $D^{eff}(33\ ms)_{100\ ms}$ (SFMT, median value) using the equation $\tau = L^2/4D_{MACRO}$ for TfR and DOPE.

T24 cells (Figure 7B, fifth pair of graphs, and Supplemetal Table S3). Because the cytoplasmic domain sizes of these two molecules are similar, the increase of the cytoplasmic domain size from 134 aa (intact dimer) to 448 aa did not change $D^{eff}(33\ ms)_{100\ ms}$ (preceding paragraph), and, as described in this article, the extracellular matrix and the extracellular domains of TfR were not involved in slowing macroscopic diffusion, we concluded that a decrease in the cross section of the TM domain greatly increases the hop frequency. This result suggests that the confining effect of pickets might be stronger than that of the actin-MSK fence for TfR in both PtK2 and T24 cells.

However, even these monomeric Halo-TfR molecules diffused slightly (but statistically significantly) more slowly than those of the acyl carrier protein (ACP)-tag protein conjugated to the TM domain of the low-density-lipoprotein receptor (Figure 7, bottom graphs, and Supplemental Table S3), a typical nonraft molecule (ACP-TM with only 10 aa in the cytoplasmic domain; Suzuki et al., 2012). This result can be explained by the fence effect on the mutant TfR-Halo monomers (381 vs. 10 aa for ACP-TM) by the actin MSK. However, it might also be due to the presence of small amounts of noncovalent dimers formed between mutant TfR-Halo and endogenous TfR. Overall these results indicate that both the fence and picket effects are important to temporarily confine TfR within a compartment, but the TM pickets bound to the actin-MSK fence are more effective than the fence itself for TfR in both PtK2 cells and T24 cells.

As extensively described here, the compartment sizes are virtually the same for TfR and gold-DOPE under all conditions examined in this study. This suggests that monomeric TfR and ACP-TM would sense the same compartment size as the native TfR (dimer) and gold-DOPE.

DISCUSSION
Actin-MSK suppressed the diffusion rates of TfR and DOPE by a factor of >17 from those in actin-free membranes. Third objective of this research
The results shown in Figure 3 indicate that both gold-DOPE and TfR undergo suppressed diffusion in the PM, which is detectable only at a very high time resolution of 0.025 ms. It is almost entirely missed at video rate observations, whereas at a 2-ms time resolution, only 33% of TfR and 12% of DOPE were classified into the suppressed-diffusion mode.

The almost complete removal of the actin-MSK (i.e., in the blebbed PM plus latrunculin A treatment) virtually abolished hop diffusion and induced very fast simple-Brownian diffusion for both TfR and DOPE, with diffusion coefficients of ~8.3 µm²/s (Supplemental Figure S5C and Table 1). This value was practically as large as the diffusion coefficients of lipids in artificial membranes (Kusumi et al., 2012) and was greater by a factor of 17–55 than those observed for Cy3-TfR and Cy3-DOPE in the intact PMs
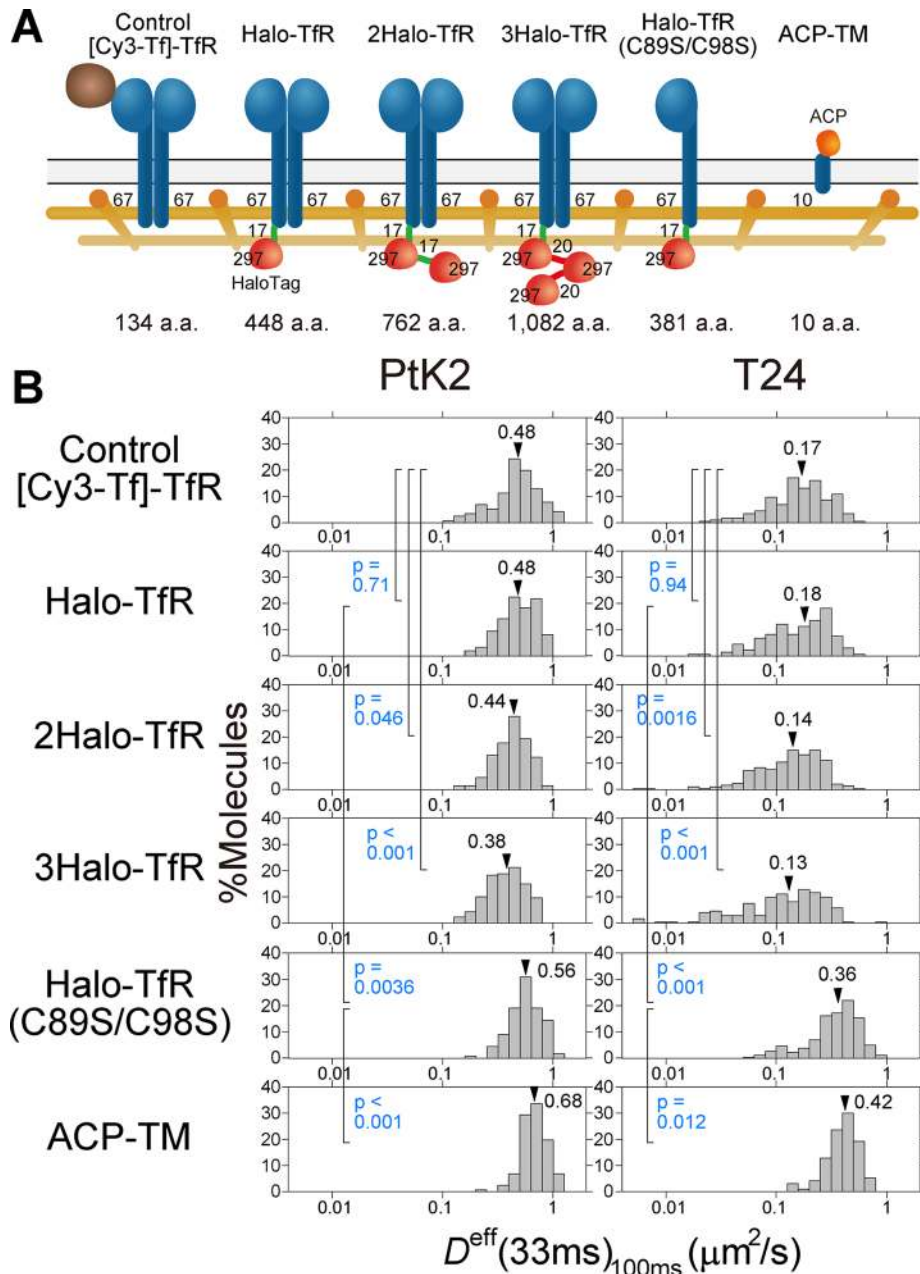
FIGURE 7: TfR's $D^{eff}(33\ ms)_{100\ ms}$ (and thus hop frequency) depends on both its cytoplasmic domain size and dimerization in both PtK2 and T24 cells. (A) Molecules used for this examination. Note that endogenous TfR exists as dimers, and that since the expression levels of modified TfR molecules are much smaller than that of endogenous TfR, most of the expressed molecules are expected to form dimers with endogenous TfR. The numbers indicate the number of amino acids in the cytoplasmic domain of the endogenous human TfR (67 aa), the Halo-tag protein (297 aa), linkers (17 and 20 aa), and the cytoplasmic domain of the ACP-TM (10 aa). The expected total numbers of amino acids in the cytoplasmic domain are shown below (the endogenous TfR in PtK2 cells was assumed to have the same number of amino acids in the cytoplasmic domain as that in human TfR). (B) Distributions of the effective macroscopic diffusion coefficient $D^{eff}(33\ ms)_{100\ ms}$ for the individual molecules in A in PtK2- and T24-cell PMs. $D^{eff}(33\ ms)_{100\ ms}$ should be proportional to the hop frequency. For a discussion of the effect of the cross section of a diffusant on its hop characteristics, see Supplemental Notes to Figure 7B.

objective of the present research), perhaps due to the crowding of TM proteins in the PM, has been proposed (Schmidt and Nichols, 2004; Lenne *et al.*, 2006; Frick *et al.*, 2007; Gambin *et al.*, 2006; Manzo *et al.*, 2011; Vicidomini *et al.*, 2011; Billaudeau *et al.*, 2013). However, this interpretation of their data is inconsistent with the present observations showing that the diffusion in the blebbed PM, with basically the same concentrations of TM proteins but very little actin-MSK, is as fast as that in artificial lipid membranes (Fujiwara *et al.*, 2002; Kusumi *et al.*, 2012).

Both lipids and TM proteins undergo hop diffusion induced by actin-MSK: equality of compartment sizes for TfR and DOPE under all of the examined conditions and their equality with actin-MSK mesh sizes. First objective of this research

Modulations of actin filaments by drug treatment induced changes in compartment size and/or residency time (Figure 6, Supplemental Figure S4, Table 2, and Supplemental Table S2). Of interest, the compartment sizes for TfR and DOPE were very similar to each other in each of the five cell lines examined (Figure 4B), although the actual compartment sizes are different from each other between these cell lines. Furthermore, when PtK2 cells and NRK cells were treated with actin-modifying drugs, the compartment sizes for TfR and DOPE were very similar to each other under examined conditions (Figure 6B, Supplemental Figure S4, Table 2, and Supplemental Table S2).

The compartment sizes determined in the PMs of PtK2 cells (this work), NRK cells, and FRSK cells (Morone *et al.*, 2006) were found to be the same as the mesh sizes of the actin-MSK located within 8.8 nm from the PM, as determined by electron tomography (Figure 5G). Taken together, these results indicate that the underlying mechanism for the hop diffusion of phospholipids and TM proteins must be the same and must involve the actin-based MSK.

How does actin-MSK induce hop diffusion of both phospholipids and TM proteins?

In the present research (Figure 7 and Supplemental Table S3), we found that an increase in TfR cytoplasmic domain size caused $D^{eff}(33\ ms)_{100\ ms}$ to be slightly but

of the five cell lines examined here (Table 1), confirming previous observations in which the diffusion in the intact PM is reduced from that in the actin-free blebbed PM by a factor of ~20.

A model of slowed simple-Brownian diffusion for phospholipids (rather than hop diffusion; testing this model was the third major

significantly reduced, suggesting that the collision of the TfR cytoplasmic domain with the actin-MSK was involved in confining TfR in the actin-MSK mesh, although this effect would be quite limited. Meanwhile, the $D^{eff}(33\ ms)_{100\ ms}$ value of monomeric TfR was much greater than that of dimeric TfR, indicating that monomeric TfR

passes compartment boundaries much more readily. These results suggest that the confining effect of pickets on TfR might be much greater than that of the fence in the PtK2-cell PM.

There is no fence effect on DOPE, and yet DOPE showed actin-dependent compartmentalization and hop diffusion, with compartment sizes the same as those detected by TfR and also same as the actin-MSK mesh sizes determined by electron tomography. Therefore we propose that DOPE confinement within compartments is induced by TM pickets anchored to the actin fence.

These results, as well as those described in the previous subsection, indicate that the second purpose of the present investigation (to examine thoroughly the PM of PtK2 cells) has been accomplished. Furthermore, both results are consistent with the recent conclusions of Andrade et al. (2015).

Biological significance of the partitioned membrane

In the present research, we were particularly concerned with three models of molecular dynamics in the PM and the PM domain structure: 1) temporary binding and/or transient entrapment within a nanoscale-domain model (Eggeling et al., 2009; Sahl et al., 2010; Honigmann et al., 2014), 2) a slow, simple-Brownian diffusion model (i.e., the third objective of the present research; Gambin et al., 2006; Frick et al., 2007), and 3) the fence-and-pickets model. Our results described here are inconsistent with models 1 and 2, even in the PtK2 cells used by Eggeling et al. (2009) and Sahl et al. (2010), as well as in the additional four cell lines. The equal compartment sizes for phospholipids and a transmembrane protein, TfR, under all conditions in the present study (intact PMs of the five cell lines and under all of the drug-induced actin modification conditions) provided confirmatory evidence in support of the fence-and-pickets model.

The hop diffusion and PM compartmentalization induced by the actin-MSK are not contrary to the fluid-mosaic model proposed by Singer and Nicolson (1972). The Singer–Nicolson model is perfectly suitable for molecular events occurring on space scales of ~10 nm, which is the scale of the original figure in their elegant report. However, the PM partitioning model proposes that, for PM molecular events occurring on greater scales, temporary confinement within a compartment and hop diffusion of molecules must be considered. This model appears to be quite broadly suitable because it is applicable to all mammalian cells examined thus far, including PtK2 cells (despite many recent publications—see Supplemental Figure S6—on why hop diffusion appears like simple-Brownian diffusion interrupted by frequent transient entrapment), and Escherichia coli (Oh et al., 2014) and to various types of molecules incorporated in the PM, including, in addition to TfR and DOPE, a G protein–coupled receptor, a μ-opioid receptor (Suzuki et al., 2005), an MHC class II protein (a transmembrane protein; Umemura et al., 2008), and a GPI-anchored protein (a mutant MHC protein class II with transmembrane domain replaced by the GPI-anchoring chain; Umemura et al., 2008), as well as to two more phospholipids, L-α-dipalmitoylphosphatidylethanolamine (DPPE) and L-α-dimyristoylphosphatidylethanolamine (DMPE) (Hiramoto-Yamaki et al., 2014).

The actin-MSK–induced PM partitioning (compartmentalization) is important for various PM functions. First, according to Kalay et al. (2012), such partitioning will not change the bimolecular collision rate (thus the reaction rate) for the entire PM since it does not affect the thermal equilibrium, but it can create local "bursting of reactions" and thus their spatial variations. Second, Iino et al. (2001) showed that in the partitioned PM, E-cadherin oligomers tend to be trapped longer, due to their increased size, within the compartment where they are formed (termed oligo-

merization-induced trapping), which might be useful for the short-term memory of the location where the ligand binding to the receptor was initially induced (Chung et al., 2010; Heinemann et al., 2013; Shelby et al., 2013; Shrivastava et al., 2013). Third, actin-MSK–induced partitioning is used to create a macroscopic diffusion barrier in the PM of the neuronal initial segment region (Nakada et al., 2003). Further studies of the PM compartmentalization mechanism and its biological functions are clearly required.

MATERIALS AND METHODS
Cell culture
NRK fibroblasts and human T24 epithelial cells were grown in Ham's F-12 medium (Sigma-Aldrich, St. Louis, MO) supplemented with 10% fetal bovine serum (FBS; Sigma-Aldrich). The T24 cells are the same as the ECV304 cells used in Murase et al. (2004), which were erroneously regarded as an endothelial cell line but were previously reported to be a subclone of T24 epithelial cells (Tanabe et al., 1999). PtK2 (rat kangaroo kidney) epithelial cells and human HeLa epithelial cells were grown in Eagle's MEM (Sigma-Aldrich) supplemented with 10% FBS, 0.1 mM nonessential amino acids (Gibco/Invitrogen, Carlsbad, CA), and 1 mM sodium pyruvate (Gibco/Invitrogen). Mouse kidney HEPA-OVA epithelial cells were grown in DMEM (Sigma-Aldrich) supplemented with 10% FBS.

All cell lines were cultured on 12-mm-diameter glass-bottom dishes (IWAKI, Tokyo, Japan) for SFMT or 18 × 18–mm coverslips (IWAKI) for SPT, and single-molecule observations were performed 2 d after inoculation. For SFMT of the PtK2, HeLa, and HEPA-OVA cells, the MEM or DMEM was replaced by Ham's F-12 medium containing 10% FBS at 1 d before observation. This procedure considerably decreased the level of autofluorescence in these cells.

Cell treatments to remove cell-surface proteins with trypsin, modulate the actin cytoskeleton, and form PM blebs
The extracellular domains of membrane proteins and the extracellular matrix were partially removed by treating cells with low concentrations of trypsin (the exact concentrations differed, depending on the cell type; see later description), in Hanks' balanced salt solution (HBSS; Nissui, Tokyo, Japan) buffered with 2 mM 1,4-piperazinediethanesulfonic acid (PIPES), pH 7.2 (HP medium), which did not detach the cells from the coverslips, using the protocols described by Fujiwara et al. (2002) and Murase et al. (2004). To monitor the extent of cleavage, the extracellular surface proteins, including both the extracellular domains of membrane proteins and extracellular matrix proteins, were first tagged with sulfosuccinimidyl-biotin (Sigma-Aldrich) and were visualized by Alexa 488–streptavidin (Molecular Probes, Eugene, OR) before and after trypsin treatment. Collagen type I was detected by the indirect immunofluorescence method, using a polyclonal rabbit anti–collagen type I antibody (Novus Biologicals, Littleton, CO) and a rhodamine–goat anti-rabbit antibody (Cappel, Irvine, CA). Chondroitin sulfate glycosaminoglycan was detected using CS-56 mouse anti–chondroitin sulfate immunoglobulin G (Seikagaku, Osaka, Japan) and a Rhodamine Red-X donkey anti-mouse antibody (Jackson ImmunoResearch, West Grove, PA). Epifluorescence images of cells were captured by MetaMorph software (Molecular Devices, Downingtown, PA), and fluorescence intensity was quantitated. When NRK cells were treated with 25 μg/ml trypsin at 37°C for 10 min, 61% of the extracellular surface proteins were removed. For the removal of 51% of the extracellular surface proteins of PtK2 cells, the required trypsin concentration was as high as 200 μg/ml (37°C for 10 min).

Cytochalasin D, latrunculin A, and jasplakinolide, kindly provided by Gerard Marriott (University of California, Berkeley, CA), were

used for the modulation of the actin cytoskeleton. Cytochalasin D caps the barbed end to block the interaction of actin with barbed end–binding proteins and inhibits the polymerization at both ends of actin filaments, whereas latrunculin A binds to actin monomers, inhibiting their participation in the actin polymerization reaction (Ayscough, 1998) and thus reducing the level of actin polymerization. Jasplakinolide stabilizes actin filaments (Bubb et al., 2000). These drug treatments were performed during observation by microscopy at 37°C, and, unless otherwise stated, single-molecule tracking experiments were initiated 5 min after adding these drugs and were completed within 10, 15, and 30 min, depending on the type of experiment.

PM blebs 5–20 μm in diameter in which the MSK was partially depleted were formed by incubating the cells with 1 mM menadione (2-methyl-1,4-naphthoquinone; Sigma-Aldrich) in HP medium at 37°C for 1 h (Malorni et al., 1991). To further remove the actin-based skeleton, the cells were then treated with latrunculin A as described.

Preparation of the fluorescence probes (Cy3-Tf, Alexa 633–Tf, and Cy3-DOPE) and cell surface labeling
Human and bovine holo-Tf were purchased from Sigma-Aldrich, Cy3-succinimidyl ester (monofunctional) was from GE Healthcare Biosciences (Pittsburgh, PA), and Alexa 633–succinimidyl ester was from Molecular Probes. To produce Cy3-Tf, 10 μl of a 6.5 mM Cy3 solution in dimethylformamide was added to 200 μl of a 0.5 mg/ml (6.3 μM) Tf solution in 0.1 M carbonate buffer (Na_2CO_3-$NaHCO_3$, pH 9.0). After an incubation for 60 min at 25°C, the unreacted dye was removed by desalting column chromatography (PD-10; GE Healthcare Biosciences), and equilibrated and eluted with phosphate-buffered saline, and the fractions of the eluate with the dye/protein ratio of 3.9/1 were collected for SFMT observations. Alexa 633–Tf was prepared in the same manner, except that the concentration of Alexa 633 in the reaction mixture was twofold higher, and the eluate with the dye/protein ratio of 7.6/1 was collected.

For SFMT observations of Cy3-Tf, after three washes with 1 ml of HP medium, the cells were incubated for 10 min at 37°C in the same medium to remove the Tf molecules prebound to TfR. Cy3-Tf (10 nM) was added to the cells to a final concentration (~0.1 nM) appropriate for single-molecule observations. The translational diffusion of Cy3-Tf bound to TfR (Cy3-TfR) was observed on the apical cell membrane at 37 ± 1°C immediately after the addition of Cy3-Tf without exchanging the medium.

Synthesis of DOPE (Avanti Polar Lipids, Alabaster, AL) conjugated with Cy3-succinimidyl ester (GE Healthcare Biosciences) in the head group region (Cy3-DOPE) and its incorporation into the PM were accomplished according to Fujiwara et al. (2002) and Murase et al. (2004).

SFMT of Cy3-Tf–labeled TfR (Cy3-TfR) and Cy3-DOPE
All observations of the cells were performed at 37 ± 1°C for up to 30 min. Individual Cy3 molecules were monitored on the upper PM at video rate (30 Hz), using the oblique illumination mode of a home-built objective lens-type total internal reflectrence microscope (Iino et al., 2001; Koyama-Honda et al., 2005). Briefly, a 532-nm laser beam (the second harmonic of the Nd:YAG laser beam; model 4501-050; Uniphase, San Jose, CA) was attenuated with neutral density filters, circularly polarized, and then steered into the edge of a high–numerical aperture (NA) oil immersion objective lens (PlanApo 100×/NA 1.45; Olympus, Tokyo, Japan), with a focus at the back-focal plane of the objective lens on an Olympus inverted microscope (IX-70).

The precision of the position determination was estimated from the SD of the coordinates of Cy3-Tf adsorbed to a poly-L-lysine–coated coverslip overlaid by a 15% polyacrylamide gel (5% cross-linker; Garcia-Parajo et al., 2000) and was ~20 nm at a time resolution of 33 ms.

To monitor the recruitment of TfR molecules into clathrin-coated pits, T24 cells were transfected with mouse placental clathrin light chain fused to enhanced GFP at the N-terminus (GFP-clathrin; a gift from J. H. Keen, Thomas Jefferson University, Philadelphia, PA; Gaidarov et al., 1999). Simultaneous observations of individual Alexa 633-Tf–labeled TfR and clusters of GFP-clathrin were performed by using the dual-color SFMT setup described by Koyama-Honda et al. (2005). The two images were spatially corrected and overlaid with an accuracy of 13 nm (Koyama-Honda et al., 2005).

Preparation of gold-Tf and cell surface labeling
Gold-Tf was prepared essentially as described by Fujiwara et al. (2002). The 40-nm-diameter colloidal gold particles (British BioCell, Cardiff, UK) conjugated with bovine Tf were prepared by mixing 50 μl of 31 μg/ml bovine Tf in 2 mM phosphate buffer, pH 7.2, and 500 μl of colloidal gold suspension (2.8 μg/ml Tf in the mixture). After incubation of the mixture for 1 h at room temperature, the gold-Tf complex was further stabilized with 0.05% Carbowax 20M (Sigma-Aldrich). After two washes by centrifugation and resuspension in 0.05% Carbowax/2 mM phosphate buffer, pH 7.2, the conjugates were resuspended in 0.05% Carbowax 20M/HBSS buffered with 2 mM PIPES, pH 7.2 (observation medium). The gold probe suspension (~0.05 nM of gold particles; 3×10^{10} particles/ml) was added to the cells that had been incubated in HP medium for 10 min at 37°C to remove the Tf molecules prebound to TfR.

To minimize the effect of cross-linking by the gold probe, the amount of Tf molecules conjugated to a gold particle was reduced until $D^{eff}(33ms)_{100ms}$ of TfR in PtK2 cells was maximized (PtK2 cells were used because they exhibited a smaller compartment size, ~45 nm, in our preliminary studies, which would make the cross-linking effect more apparent) while maintaining the number of Gold-Tf molecules specifically bound to the cell surface at a sufficient level for experimental purposes. With a reduction in the Tf concentration incubated with colloidal gold particles, $D^{eff}(33 ms)_{100 ms}$ was increased and leveled off at 0.30 μm²/s at a Tf concentration of ~2.8 μg/ml. These gold probes exhibited a ratio of specific (Tf-conjugated) versus nonspecific (without Tf conjugation) binding to the PtK2 cells of 4:1 (12.0 vs. 3.0 particles/cell on average). Further reduction of the number of Tf molecules on the gold particle did not substantially increase the diffusion coefficient but did decrease the fraction of specifically bound gold particles, and therefore we used these conditions for the preparation of Gold-Tf throughout this research.

Preparation of colloidal gold probes for DOPE diffusion in the PM
The preparation of 40-nm-diameter colloidal gold particles conjugated with the Fab fragments of anti-fluorescein antibodies (Molecular Probes), the fluorescein-DOPE synthesis, and the optimization of labeling conditions were performed according to Fujiwara et al. (2002) and Murase et al. (2004). The gold probe suspension (~0.05 nM of gold particles) was added to cells that had been preincubated with fluorescein-DOPE, and the translational diffusion of DOPE was recorded immediately after the binding of the gold probe to the fluorescein-DOPE incorporated in the PM.

Murase et al. (2004) found that on longer time scales, such as 3 s, the average $D^{eff}(33 ms)_{1.5 s}$ for Gold-DOPE was smaller than that for

Cy3-DOPE by a factor of two to three and concluded that this is induced by cross-linking of DOPE by colloidal gold probes. Therefore, in previous and present studies, the gold probes were optimized by reducing the number of molecules attached to the gold particle so that the effective diffusion coefficient was maximized under conditions in which the specificity of the probe binding was maintained (specific vs. nonspecific binding to the cell surface was 4:1; Fujiwara et al., 2002; Murase et al., 2004).

The gold particles bound to DOPE did not interact with either the extracellular matrix proteins or the extracellular domains of membrane proteins, which might hinder the diffusion of gold-tagged DOPE more than nonlabeled DOPE, because Fujiwara et al. (2002) and Murase et al. (2004) found that the trypsin treatment, which removed ~60–85% of the extracellular matrix proteins and the extracellular domains of membrane proteins, did not affect the diffusion of Gold-DOPE.

SPT of gold-Tf–labeled TfR and gold-DOPE
For the observations with enhanced frame rates, a digital high-speed camera with a C-MOS sensor was used (FASTCAM-ultima; Photron, Tokyo, Japan; Tomishige et al., 1998; Fujiwara et al., 2002). For high-speed videomicroscopy of colloidal gold–labeled molecules, bright-field optical microscopy was used, using a Zeiss Axioplan upright microscope equipped with an αPlan-Fluar 100× oil immersion objective lens (NA 1.45). The sequence of images was replayed at the video rate (30 Hz) with analogue and digital enhancement by an image processor (DVS-3000; Hamamatsu Photonics, Hamamatsu, Japan) and recorded on a digital videotape recorder (DSR-20; Sony, Tokyo, Japan).

The precision of the position determination was estimated by the same method used in SFMT using 40-nm-diameter gold particles and was 17 nm at a time resolution of 25 μs (Fujiwara et al., 2002).

Obtaining the trajectories of membrane molecules and plots of MSD versus time
All of the probes observed in the image were used for analysis, without any arbitrary selection by the observers. The positions (x- and y-coordinates) of each gold particle and each fluorescent molecule were determined by an in-house computer program that uses the method developed by Gelles et al. (1988). For each trajectory, the MSD for every time interval was calculated according to the following formula (Qian et al., 1991; Kusumi et al., 1993):

$$MSD(N,n) = MSD_x(N,n) + MSD_y(N,n)$$
$$= \frac{1}{N-1-n}\sum_{j=1}^{N-1-n}\{[x(j+n)-x(j)]^2 + [y(j+n)-y(j)]^2\} \quad (1)$$

where δt is the video frame time; (x(j + n), y(j + n)) describes the particle position after a time interval nδt after starting at position (x(j), y(j)); N is the total number of frames in the video recording sequence; n and j are positive integers; and n determines the time increment.

Classification of the mode of diffusion, calculation of the diffusion coefficient, and analysis of high-speed SPT trajectories
For a detailed description of the data analysis methods, see Fujiwara et al. (2002) and Suzuki et al. (2005). Anomaly in diffusion is often described using the anomaly factor α, assuming that ln[MSD(t)] is proportional to α ln(t). However, this method generally neglects complicated causes of anomaly (and thus more compli-

cated time dependence), and it almost always neglects the time scale for the analysis. Thus the types of anomalous diffusion for which it is useful are quite limited (Saxton, 2012). Therefore, in the present research, we used the following method, which we developed previously.

A statistical method for classifying each trajectory into the suppressed-diffusion mode, the simple-Brownian-diffusion mode, the mode of simple-Brownian diffusion with drift, or the immobile mode, based on the MSD–Δt plot was described by Kusumi et al. (1993). Briefly, all of the trajectories were first classified into either the mobile or immobile mode, and the mode-of-motion classification was performed only for the trajectories that were classified as mobile (see Figure 2B and the related discussion in the Results section).

The classification was performed based on the RD value, defined as

$$RD(N,n) = \frac{MSD(N,n)}{4Dn\delta t} \quad (2)$$

with $D_x = D_y = D$ for simple-Brownian diffusion. The ensemble-averaged RD is <<, ≈, or >> 1 when the molecules are undergoing suppressed diffusion, simple-Brownian diffusion, or simple-Brownian diffusion with drift (directed diffusion mode), respectively. Figure 2B shows the theoretical curves for 1) simple-Brownian diffusion, for which MSD(Δt) = 4DΔt, 2) the directed-diffusion mode, in which a molecule moves in a direction at a constant drift velocity (v_x, v_y) with superimposed random diffusion, MSD(Δt) = 4DΔt + $v^2(\Delta t)^2$, where $v^2 = v_x^2 + v_y^2$, and 3) suppressed (totally confined) diffusion, in which a molecule undergoes Brownian diffusion while totally confined within a limited area (compartment; 0 ≤ x ≤ L_x, 0 ≤ y ≤ L_y) during the observation period. The MSD–Δt plot levels off and asymptotically approaches a constant value, as expressed by

$$MSD_x(N,n) = \frac{L_x^2}{6} - \frac{16L_x^2}{\pi^4}\sum_{k=1(odd)}^{\infty}\frac{1}{k^4}\exp\left\{-\frac{1}{2}\left(\frac{k\pi\sigma_x}{L_x}\right)^2\right\}$$
$$MSD_y(N,n) = \frac{L_y^2}{6} - \frac{16L_y^2}{\pi^4}\sum_{k=1(odd)}^{\infty}\frac{1}{k^4}\exp\left\{-\frac{1}{2}\left(\frac{k\pi\sigma_y}{L_y}\right)^2\right\} \quad (3)$$
$$\sigma_x^2 = 2D_xn\delta t, \ \sigma_y^2 = 2D_yn\delta t, \quad 4D = 2D_x + 2D_y$$
$$L_y^2 = L_x^2 + L_y^2$$

For the analysis of the trajectories obtained by using high-speed SPT with 0.025-ms resolution and classified into the suppressed-diffusion mode (under the analysis conditions used therein), the MSD–Δt plots in the x- or y-direction was fitted with an in-house program based on the hop diffusion theory of Powles et al. (1992), in which a particle undergoes diffusion in the presence of semipermeable barriers placed at an equal distance (termed "hop fitting" in the present article; Fujiwara et al., 2002; Murase et al., 2004; Suzuki et al., 2005). See the Results for further details.

The correct hop rate (or the residency time within a compartment) was evaluated from the macroscopic diffusion coefficient, determined by SFMT with a fluorescent probe, and the compartment size was determined by SPT with a gold probe. Individual compartments for each trajectory were automatically identified by the computer program (Kusumi et al., 2005; Suzuki et al., 2005).

The following points must be considered with any hop fitting, but they become especially important when very short residency times within each compartment or very small compartment sizes are expected.

As discussed in Suzuki et al. (2005), 1) the total period of the trajectory used for the MSD calculation must be long enough so that

a target molecule exhibits a jump (jumps) between the compartments, and 2) the frame rate must be sufficiently high so that a target molecule stays in each compartment for a period of several tens of frames on average. Therefore, when the residency time within each compartment (τ) is expected to be as short as 1–10 ms, we argue that each observation period (total duration of the observation) should be >1.5–15 ms (1.5τ) and the frame rate should be greater than one frame per 0.03–0.3 ms (τ/30).

In addition, 3) the time window of the MSD–Δt plot needs to be properly determined so that the contributions from D_{micro} (the initial slope) and D_{MACRO} (the slope toward the end of the plot) to the MSD–Δt curve are well balanced. Therefore, for TfR and DOPE molecules in PtK2 cells, the total observation period of 12 ms (to fulfill requirement 1), the time resolution of 0.025 ms (requirement 2), and the MSD–Δt time window of 1.5 ms (requirement 3) were selected. Although a 1.5-ms time window may seem too short to detect hops every ~2 ms, all of the possible pairs in the whole 12-ms trajectory are used to calculate the MSD value for each time interval, and therefore this time window would contain sufficient information to successfully estimate the hop parameters.

Finally, 4) the contribution from the Gaussian position determination errors to the MSD–Δt plot must be subtracted to estimate the compartment size correctly. Even in single-particle tracking with subpixel precision in particle positions, such as that used here, all of the MSDs include Gaussian position determination errors attributable to the systematic pixelation of the camera and the random noise derived from the optics, the detector, and the sample, and these errors must be subtracted. The SD of this Gaussian error for gold particles fixed on a coverslip was 17 nm on average at a 0.025-ms frame time (for one dimension; Fujiwara et $al.$, 2002). This means that the correct compartment sizes for TfR and DOPE molecules in PtK2 cells should be slightly smaller than those (100 nm or a little smaller) predicted from the visual inspection of the trajectories (Figure 3A, bottom). When the trajectory is long enough so that the statistical variation in the MSD values is sufficiently reduced, this Gaussian position determination error appears on the MSD–Δt plot as an offset—a constant value irrespective of the time interval (2 × SD^2 for one dimension; Dietrich et $al.$, 2002; Martin et $al.$, 2002). Therefore, to estimate the correct (average) compartment size for each trajectory, the offset value was determined as the y-intercept (x = 0) in the MSD–Δt plot and was subtracted (the intercept was found by extrapolating the linear-fit function for the first, second, and third data points in the MSD–Δt plot for each direction). The two-dimensional MSD–Δt plot shown in Figure 4A is that after the subtraction of the offset. The two-dimensional offset value is the sum of those for the x- and y- directions. The experimentally determined one-dimensional value was 742 nm^2 (n = 108; i.e., x- and y-axes for 54 TfR trajectories), giving a position determination error of (742/2)$^{1/2}$ = 19.3 nm on average. This is in good agreement with the value of 17 nm obtained for gold particles fixed on a coverslip, thus showing that the offset values were properly determined on the PM.

Theoretical distribution of RD values for particles undergoing simple-Brownian diffusion

Here we describe an analytical approximation for the distribution of RD(N, n) given in Eq. 2. To perform the calculations, we consider the large-N limit, where trajectories are long enough that the estimated values of D can be approximated by a constant. Therefore the distribution of RD(N, n) is simply proportional to the distribution of MSD.

MSD(N, n) can be calculated in two ways (Saxton, 1997): averaging squared displacements over a time interval $n\delta t$ by either allowing overlapping intervals (as in Eq. 1) or using only nonoverlapping (independent) intervals. Here we employ the second strategy because it has the advantage that the distribution of the MSD can be calculated exactly (Qian et $al.$, 1991; Saxton, 1997). In this case, the MSD is given by

$$MSD'(N,n) = \frac{1}{K}\sum_{k=0}^{K-1}\{[W_x(1+kn,n(k+1))]^2 + [W_y(1+kn,n(k+1))]^2\} \quad (4)$$

where $W_z(i, j)$ is the displacement between the (j + 1)th and ith frames along the z-axis ($j \geq i$) and K is the number of nonoverlapping intervals, being the largest integer $\leq(N-1)/n$. Under the assumption of simple-Brownian motion, $W_z(i, j)$ is a Gaussian random variable whose mean is zero and variance is equal to 2($j - i + 1$)$D\delta t$, since the displacement between consecutive time steps is Gaussian with zero mean and variance equal to 2$D\delta t$.

Because the W_z in Eq. 4 can be treated as independent Gaussian random variables, we can write

$$MSD'(N,n) = \frac{n\sigma^2}{K}\sum_{k=0}^{K-1}\left[\left(\frac{N(0,n\sigma^2)}{\sqrt{n\sigma^2}}\right)^2 + \left(\frac{N(0,n\sigma^2)}{\sqrt{n\sigma^2}}\right)^2\right] \quad (5)$$

where $\sigma^2 = 2D\delta t$ and $N(a, b)$ denotes a Gaussian random variable of mean a and variance b. Because $N(0, n\sigma^2)/(n\sigma^2)^{1/2}$ is Gaussian distributed with unit variance, its square follows the chi-squared distribution, and the sum of m chi-squared variables is still chi-squared with m degrees of freedom. Therefore we finally have

$$MSD'(N,n) = \frac{n\sigma^2}{K}\chi^2(2K) \quad (6)$$

where $\chi^2(m)$ is a chi-squared distributed random variable with m degrees of freedom. Using the properties of $\chi^2(m)$, we can express the probability density function of MSD' as

$$f_{MSD'}(x;N,n) = \frac{K}{n\sigma^2}\frac{1}{2^K(K-1)!}\left(\frac{Kx}{n\sigma^2}\right)^{K-1}\exp\left(-\frac{Kx}{2n\sigma^2}\right) \quad (7)$$

Finally, we arrive at the distribution of RD(N, n) by noting that RD(N, n) = MSD/(4$Dn\delta t$), which means that the probability distribution function of RD(N, n) can be obtained from Eq. 7 via rescaling x by the factor 1/(4$Dn\delta t$) and dividing the resulting expression by the same factor. Therefore the probability density function of RD(N, n) is also chi-squared distributed and is explicitly given by

$$f_{RD}(x;N,n) = \frac{K}{(K-1)!}(Kx)^{K-1}\exp(-Kx) \quad (8)$$

Note that the chi-squared distribution approaches a Gaussian distribution for large values of m, via the central limit theorem. Because RD(N, n) is proportional to a chi-squared distribution with ~2(N–1)/n degrees of freedom (see Eq. 6), we expect the RD(N, n) distribution to look like a Gaussian distribution at small values of n (2(N–1)/n >> 1), and to be more skewed at large values of n (2(N–1)/n ~ 1). In Supplemental Figure S2, we compare the distribution of RD(N, n) obtained by using the results of Monte Carlo simulations of simple-Brownian motion to that calculated by Eq. 8. See the legend to the figure for parameter values.

Rapid-freeze, deep-etch, and platinum-replica electron microscopy of the PM cytoplasmic surface

The method used was virtually the same as that used previously (Morone et $al.$, 2006). Briefly, the cytoplasmic surface of the upper PM (apical PM with scarce microvilli) of PtK2 cells (grown to ~60%

confluency) was exposed by removing the apical PM from the rest of the cell. This was performed in the following manner. After coverslips coated with positively charged Alcian blue 8GX (Wako, Tokyo, Japan) were placed on top of the cell layer and incubated at 4°C for 15 min, the coverslips were gently floated off from the cells using the surface tension of the buffer by slowly adding ice-cold PIPES buffer containing 1% paraformaldehyde/0.25% glutaraldehyde into the space between the culture dish and the coverslip. When the coverslip floated off, the cells were cleaved, and the upper PM remained attached to the coverslip.

Each coverslip was placed on the plunger tip of the rapid-freezing device (Eiko, Tokyo, Japan) with the cytoplasmic surface of the membrane facing down. The specimen was slammed down (free fall) onto a polished, pure-copper block, which was prechilled by direct immersion in liquid helium. The excess ice on the cytoplasmic surface was shaved off, and the cytoplasmic surface was etched and then rotary shadowed with platinum at an angle of 22.5° from the surface (FR7000-S; Hitachi, Ibaraki, Japan). The replicas were removed from the glass surface and mounted on 100–200 mesh copper grids (Ted Pella) coated with polyvinyl formvar (Nisshin EM, Tokyo, Japan).

Electron tomography

For three-dimensional (3D) reconstruction, the replica was imaged at tilt angles of every 1.0° in the range ±70° (total 141 images) for a single field by a Tecnai Sphera F20 transmission electron microscope (FEI, Eindhoven, Netherlands) equipped with a charge-coupled device camera (1024 ×1024 pixels). The pixel size at the specimen was 1.1 nm. The image acquisition was fully automated, as previously described (Medalia et al., 2002). The 100–121 image sections of every 1.1 nm were obtained by a calculation based on the set of 141 tilt images using the IMOD software package (Kremer et al., 1996) running on Linux. Corrections for the tilt of the specimen and the long-wavelength undulations of the membrane were also accomplished with the IMOD software. The 3D rendering (displaying 3D images in different ways) was performed using the Mercury Computer Systems AMIRA DEV software package (San Diego, CA) operating on a Linux system.

The thickness (width in the image) of the actin filament after platinum shadowing was between 9 and 11 nm (Heuser, 1983), and the thickness of the platinum replica was ≤2 nm (Heuser, 1983; Moritz et al., 2000), and thus the height of the actin filament associated with the membrane was 7–9 nm (because the height is given by the actin thickness and one replica thickness, whereas the width in the image is determined by the actin thickness plus two replica thicknesses), with 8 nm being a reasonable estimate. In the series of electron tomography sections shown in Figure 5, A and B, two major classes of filaments with regard to the distance from the membrane surface can be discerned (a third class of filaments, localized >15.4 nm from the PM cytoplasmic surface, also exists but is not visible in Figure 5, A and B).

The first class of filaments is distinct even in the first 0- to 2.2-nm section in the computer-reconstructed sections (because the contrast is reversed in these micrographs, they look more lucent or white), but fade out in the sections of 8.8–11.0 or 11.0–13.2 nm from the PM inner surface. These filaments are colored green in Figure 5C. We consider these filaments to be in direct contact with the PM (the gap between the filament and the inner membrane surface is <1.1 nm) because they can be seen clearly even in the first 1.1-nm section. These filaments are likely to be the significant ones for generating membrane corrals.

The second class of filaments includes those that are clear in the first and/or second sections (0–2.2, 0–4.4, and 2.2–4.4 nm) from the

membrane surface and do not fade out even in the section 13.2–15.4 nm from the surface. These filaments are colored red in Figure 5C. These might be the actin filaments that had platinum coatings all around their surfaces, because they slightly stood off from the surface. We did not consider these filaments to be close enough to generate membrane corrals.

At variance with the electron tomography images obtained for the PM cytoplasmic surface of NRK cells, the first and second classes of actin filaments in the MSK of PtK2 cells are often aligned closely, as seen in Figure 5, A–E, and difficult to discern in these figures. However, by following each individual filament in three dimensions (looking at adjacent sections up and down), the filaments belonging to the first and second classes could be determined (the 0- to 8.8-nm section shown in Figure 5D).

Therefore we considered that only the first class of filaments (those colored green in Figure 5, C and E) form the MSK fences, and the areas surrounded by these filaments are colored green in the 0- to 8.8-nm section shown in Figure 5F. Note that certain areas were excluded from this analysis, including those where bundles of actin filaments are present, the actin filaments are too crowded to be individually discerned, an actin filament is terminated in the middle of a domain (domains that contain a loose end of an actin filament), or CCPs, caveolae, and smooth surface membrane invaginations are present.

REFERENCES

Andrade DM, Clausen MP, Keller J, Mueller V, Wu C, Bear JE, Hell SW, Lagerholm BC, Eggeling C (2015). Cortical actin networks induce spatiotemporal confinement of phospholipids in the plasma membrane—a minimally invasive investigation by STED-FCS. Sci Rep 5, 11454.

Ayscough K (1998). Use of latrunculin-A, an actin monomer-binding drug. Methods Enzymol 298, 18–25.

Billaudeau C, Mailfert S, Trombik T, Bertaux N, Rouger V, Hamon Y, He HT, Marguet D (2013). Probing the plasma membrane organization in living cells by spot variation fluorescence correlation spectroscopy. Methods Enzymol 519, 277–302.

Bubb MR, Spector I, Beyer BB, Fosen KM (2000). Effects of jasplakinolide on the kinetics of actin polymerization. An explanation for certain in vivo observations. J Biol Chem 275, 5163–5170.

Chaudhuri A, Bhattacharya B, Gowrishankar K, Mayor S, Rao M (2011). Spatiotemporal regulation of chemical reactions by active cytoskeletal remodeling. Proc Natl Acad Sci USA 108, 14825–14830.

Chung I, Akita R, Vandlen R, Toomre D, Schlessinger J, Mellman I (2010). Spatial control of EGF receptor activation by reversible dimerization on living cells. Nature 464, 783–787.

Cocucci E, Aguet F, Boulant S, Kirchhausen T (2012). The first five seconds in the life of a clathrin-coated pit. Cell 150, 495–507.

Costa MN, Radhakrishnan K, Edwards JS (2011). Monte Carlo simulations of plasma membrane corral-induced EGFR clustering. J Biotechnol 151, 261–270.

Costa MN, Radhakrishnan K, Wilson BS, Vlachos DG, Edwards JS (2009). Coupled stochastic spatial and non-spatial simulations of ErbB1 signaling pathways demonstrate the importance of spatial organization in signal transduction. PLoS One 4, e6316.

Day CA, Kenworthy AK (2012). Mechanisms underlying the confined diffusion of cholera toxin B-subunit in intact cell membranes. PLoS One 7, e34923.

Dietrich C, Yang B, Fujiwara T, Kusumi A, Jacobson K (2002). Relationship of lipid rafts to transient confinement zones detected by single particle tracking. Biophys J 82, 274–284.

Di Rienzo C, Gratton E, Beltram F, Cardarelli F (2013). Fast spatiotemporal correlation spectroscopy to determine protein lateral diffusion laws in live cell membranes. Proc Natl Acad Sci USA 110, 12307–12312.

Eggeling C, Ringemann C, Medda R, Schwarzmann G, Sandhoff K, Polyakova S, Belov VN, Hein B, von Middendorff C, Schonle A, et al. (2009). Direct observation of the nanoscale dynamics of membrane lipids in a living cell. Nature 457, 1159–1162.

Ehrlich M, Boll W, Van Oijen A, Hariharan R, Chandran K, Nibert ML, Kirchhausen T (2004). Endocytosis by random initiation and stabilization of clathrin-coated pits. Cell 118, 591–605.

Frick M, Schmidt K, Nichols BJ (2007). Modulation of lateral diffusion in the plasma membrane by protein density. Curr Biol 17, 462–467.

Fujiwara T, Ritchie K, Murakoshi H, Jacobson K, Kusumi A (2002). Phospholipids undergo hop diffusion in compartmentalized cell membrane. J Cell Biol 157, 1071–1081.

Gaidarov I, Santini F, Warren RA, Keen JH (1999). Spatial control of coated-pit dynamics in living cells. Nat Cell Biol 1, 1–7.

Gambin Y, Lopez-Esparza R, Reffay M, Sierecki E, Gov NS, Genest M, Hodges RS, Urbach W (2006). Lateral mobility of proteins in liquid membranes revisited. Proc Natl Acad Sci USA 103, 2098–2102.

Garcia-Parajo MF, Segers-Nolten GM, Veerman JA, Greve J, van Hulst NF (2000). Real-time light-driven dynamics of the fluorescence emission in single green fluorescent protein molecules. Proc Natl Acad Sci USA 97, 7237–7242.

Gelles J, Schnapp BJ, Sheetz MP (1988). Tracking kinesin-driven movements with nanometre-scale precision. Nature 331, 450–453.

Gowrishankar K, Ghosh S, Saha S, C R, Mayor S, Rao M (2012). Active remodeling of cortical actin regulates spatiotemporal organization of cell surface molecules. Cell 149, 1353–1367.

Heinemann F, Vogel SK, Schwille P (2013). Lateral membrane diffusion modulated by a minimal actin cortex. Biophys J 104, 1465–1475.

Heuser JE (1983). Procedure for freeze-drying molecules adsorbed to mica flakes. J Mol Biol 169, 155–195.

Hiramoto-Yamaki N, Tanaka KA, Suzuki KG, Hirosawa KM, Miyahara MS, Kalay Z, Tanaka K, Kasai RS, Kusumi A, Fujiwara TK (2014). Ultrafast diffusion of a fluorescent cholesterol analog in compartmentalized plasma membranes. Traffic 15, 583–612.

Honigmann A, Sadeghi S, Keller J, Hell SW, Eggeling C, Vink R (2014). A lipid bound actin meshwork organizes liquid phase separation in model membranes. Elife 3, e01671.

Iino R, Koyama I, Kusumi A (2001). Single molecule imaging of green fluorescent proteins in living cells: E-cadherin forms oligomers on the free cell surface. Biophys J 80, 2667–2677.

Jaqaman K, Grinstein S (2012). Regulation from within: the cytoskeleton in transmembrane signaling. Trends Cell Biol 22, 515–526.

Kalay Z, Fujiwara TK, Kusumi A (2012). Confining domains lead to reaction bursts: reaction kinetics in the plasma membrane. PLoS One 7, e32948.

Kalay Z, Fujiwara TK, Otaka A, Kusumi A (2014). Lateral diffusion in a discrete fluid membrane with immobile particles. Phys Rev E 89, 022724.

Klotzsch E, Schütz GJ (2013). A critical survey of methods to detect plasma membrane rafts. Phil Trans R Soc B 368, 20120033.

Koyama-Honda I, Ritchie K, Fujiwara T, Iino R, Murakoshi H, Kasai RS, Kusumi A (2005). Fluorescence imaging for monitoring the colocalization of two single molecules in living cells. Biophys J 88, 2126–2136.

Kremer JR, Mastronarde DN, McIntosh JR (1996). Computer visualization of three-dimensional image data using IMOD. J Struct Biol 116, 71–76.

Kusumi A, Fujiwara TK, Chadda R, Xie M, Tsunoyama TA, Kalay Z, Kasai RS, Suzuki KG (2012). Dynamic organizing principles of the plasma membrane that regulate signal transduction: commemorating the fortieth anniversary of Singer and Nicolson's fluid-mosaic model. Annu Rev Cell Dev Biol 28, 215–250.

Kusumi A, Nakada C, Ritchie K, Murase K, Suzuki K, Murakoshi H, Kasai RS, Kondo J, Fujiwara T (2005). Paradigm shift of the plasma membrane concept from the two-dimensional continuum fluid to the partitioned fluid: high-speed single-molecule tracking of membrane molecules. Annu Rev Biophys Biomol Struct 34, 351–378.

Kusumi A, Sako Y, Yamamoto M (1993). Confined lateral diffusion of membrane receptors as studied by single particle tracking (nanovid microscopy). Effects of calcium-induced differentiation in cultured epithelial cells. Biophys J 65, 2021–2040.

Kusumi A, Suzuki KG, Kasai RS, Ritchie K, Fujiwara TK (2011). Hierarchical mesoscale domain organization of the plasma membrane. Trends Biochem Sci 36, 604–615.

Lenne PF, Wawrezinieck L, Conchonaud F, Wurtz O, Boned A, Guo XJ, Rigneault H, He HT, Marguet D (2006). Dynamic molecular confinement in the plasma membrane by microdomains and the cytoskeleton meshwork. EMBO J 25, 3245–3256.

Loerke D, Mettlen M, Yarar D, Jaqaman K, Jaqaman H, Danuser G, Schmid SL (2009). Cargo and dynamin regulate clathrin-coated pit maturation. PLoS Biol 7, e57.

Malorni W, Iosi F, Mirabelli F, Bellomo G (1991). Cytoskeleton as a target in menadione-induced oxidative stress in cultured mammalian cells: alterations underlying surface bleb formation. Chem Biol Interact 80, 217–236.

Manzo C, van Zanten TS, Garcia-Parajo MF (2011). Nanoscale fluorescence correlation spectroscopy on intact living cell membranes with NSOM probes. Biophys J 100, L8–L10.

Martin DS, Forstner MB, Kas JA (2002). Apparent subdiffusion inherent to single particle tracking. Biophys J 83, 2109–2117.

Mashanov GI, Molloy JE (2007). Automatic detection of single fluorophores in live cells. Biophys J 92, 2199–2211.

Medalia O, Weber I, Frangakis AS, Nicastro D, Gerisch G, Baumeister W (2002). Macromolecular architecture in eukaryotic cells visualized by cryoelectron tomography. Science 298, 1209–1213.

Moritz M, Braunfeld MB, Guenebaut V, Heuser J, Agard DA (2000). Structure of the gamma-tubulin ring complex: a template for microtubule nucleation. Nat Cell Biol 2, 365–370.

Morone N, Fujiwara T, Murase K, Kasai RS, Ike H, Yuasa S, Usukura J, Kusumi A (2006). Three-dimensional reconstruction of the membrane skeleton at the plasma membrane interface by electron tomography. J Cell Biol 174, 851–862.

Murase K, Fujiwara T, Umemura Y, Suzuki K, Iino R, Yamashita H, Saito M, Murakoshi H, Ritchie K, Kusumi A (2004). Ultrafine membrane compartments for molecular diffusion as revealed by single molecule techniques. Biophys J 86, 4075–4093.

Nakada C, Ritchie K, Oba Y, Nakamura M, Hotta Y, Iino R, Kasai RS, Yamaguchi K, Fujiwara T, Kusumi A (2003). Accumulation of anchored proteins forms membrane diffusion barriers during neuronal polarization. Nat Cell Biol 5, 626–632.

Nicolson GL (2014). The Fluid-Mosaic Model of Membrane Structure: still relevant to understanding the structure, function and dynamics of biological membranes after more than 40 years. Biochim Biophys Acta 1838, 1451–1466.

Nishimura SY, Vrljic M, Klein LO, McConnell HM, Moerner WE (2006). Cholesterol depletion induces solid-like regions in the plasma membrane. Biophys J 90, 927–938.

Oh D, Yu Y, Lee H, Wanner BL, Ritchie K (2014). Dynamics of the serine chemoreceptor in the Escherichia coli inner membrane: a high-speed single-molecule tracking study. Biophys J 106, 145–153.

Owen DM, Williamson D, Rentero C, Gaus K (2009). Quantitative microscopy: protein dynamics and membrane organisation. Traffic 10, 962–971.

Parton RG, del Pozo MA (2013). Caveolae as plasma membrane sensors, protectors and organizers. Nat Rev Mol Cell Biol 14, 98–112.

Powles JG, Mallett MJD, Rickayzen G, Evans WAB (1992). Exact analytic solutions for diffusion impeded by an infinite array of partially permeable barriers. Proc R Soc Lond A 436, 391–403.

Qian H, Sheetz MP, Elson EL (1991). Single particle tracking. Analysis of diffusion and flow in two-dimensional systems. Biophys J 60, 910–921.

Saffman PG, Delbrück M (1975). Brownian motion in biological membranes. Proc Natl Acad Sci USA 72, 3111–3113.

Sahl SJ, Leutenegger M, Hilbert M, Hell SW, Eggeling C (2010). Fast molecular tracking maps nanoscale dynamics of plasma membrane lipids. Proc Natl Acad Sci USA 107, 6829–6834.

Saxton MJ (1982). Lateral diffusion in an archipelago. Effects of impermeable patches on diffusion in a cell membrane. Biophys J 39, 165–173.

Saxton MJ (1997). Single-particle tracking: the distribution of diffusion coefficients. Biophys J 72, 1744–1753.

Saxton MJ (2012). Wanted: a positive control for anomalous subdiffusion. Biophys J 103, 2411–2422.

Schmidt K, Nichols BJ (2004). A barrier to lateral diffusion in the cleavage furrow of dividing mammalian cells. Curr Biol 14, 1002–1006.

Sezgin E, Levental I, Grzybek M, Schwarzmann G, Mueller V, Honigmann A, Belov VN, Eggeling C, Coskun U, Simons K, et al. (2012). Partitioning, diffusion, and ligand binding of raft lipid analogs in model and cellular plasma membranes. Biochim Biophys Acta 1818, 1777–1784.

Shelby SA, Holowka D, Baird B, Veatch SL (2013). Distinct stages of stimulated FceRI receptor clustering and immobilization are identified through superresolution imaging. Biophys J 105, 2343–2354.

Shibata AC, Chen LH, Nagai R, Ishidate F, Chadda R, Miwa Y, Naruse K, Shirai YM, Fujiwara TK, Kusumi A (2013). Rac1 recruitment to the archipelago structure of the focal adhesion through the fluid membrane as revealed by single-molecule analysis. Cytoskeleton 70, 161–177.

Shibata AC, Fujiwara TK, Chen L, Suzuki KG, Ishikawa Y, Nemoto YL, Miwa Y, Kalay Z, Chadda R, Naruse K, et al. (2012). Archipelago architecture of the focal adhesion: membrane molecules freely enter and exit from the focal adhesion zone. Cytoskeleton 69, 380–392.

Shrivastava AN, Kowalewski JM, Renner M, Bousset L, Koulakoff A, Melki R, Giaume C, Triller A (2013). b-amyloid and ATP-induced diffusional trapping of astrocyte and neuronal metabotropic glutamate type-5 receptors. Glia 61, 1673–1686.

Singer SJ, Nicolson GL (1972). The fluid mosaic model of the structure of cell membranes. Science 175, 720–731.

Suzuki KG, Fujiwara TK, Edidin M, Kusumi A (2007b). Dynamic recruitment of phospholipase Cg at transiently immobilized GPI-anchored receptor clusters induces IP_3-Ca^{2+} signaling: single-molecule tracking study 2. J Cell Biol 177, 731–742.

Suzuki KG, Fujiwara TK, Sanematsu F, Iino R, Edidin M, Kusumi A (2007a). GPI-anchored receptor clusters transiently recruit Lyn and Ga for temporary cluster immobilization and Lyn activation: single-molecule tracking study 1. J Cell Biol 177, 717–730.

Suzuki KG, Kasai RS, Hirosawa KM, Nemoto YL, Ishibashi M, Miwa Y, Fujiwara TK, Kusumi A (2012). Transient GPI-anchored protein homodimers are units for raft organization and function. Nat Chem Biol 8, 774–783.

Suzuki K, Ritchie K, Kajikawa E, Fujiwara T, Kusumi A (2005). Rapid hop diffusion of a G-protein-coupled receptor in the plasma membrane as revealed by single-molecule techniques. Biophys J 88, 3659–3680.

Tanabe H, Takada Y, Minegishi D, Kurematsu M, Masui T, Mizusawa H (1999). Cell line individualization by STR multiplex system in the cell bank found cross-contamination between ECV304 and EJ-1/T24. Tissue Cult Res Commun 18, 329–338.

Taylor MJ, Perrais D, Merrifield CJ (2011). A high precision survey of the molecular dynamics of mammalian clathrin-mediated endocytosis. PLoS Biol 9, e1000604.

Tomishige M, Sako Y, Kusumi A (1998). Regulation mechanism of the lateral diffusion of band 3 in erythrocyte membranes by the membrane skeleton. J Cell Biol 142, 989–1000.

Treanor B, Depoil D, Gonzalez-Granja A, Barral P, Weber M, Dushek O, Bruckbauer A, Batista FD (2010). The membrane skeleton controls diffusion dynamics and signaling through the B cell receptor. Immunity 32, 187–199.

Umemura YM, Vrljic M, Nishimura SY, Fujiwara TK, Suzuki KG, Kusumi A (2008). Both MHC class II and its GPI-anchored form undergo hop diffusion as observed by single-molecule tracking. Biophys J 95, 435–450.

Vereb G, Szollosi J, Matko J, Nagy P, Farkas T, Vigh L, Matyus L, Waldmann TA, Damjanovich S (2003). Dynamic, yet structured: the cell membrane three decades after the Singer-Nicolson model. Proc Natl Acad Sci USA 100, 8053–8058.

Vicidomini G, Moneron G, Han KY, Westphal V, Ta H, Reuss M, Engelhardt J, Eggeling C, Hell SW (2011). Sharper low-power STED nanoscopy by time gating. Nat Methods 8, 571–573.

Vrljic M, Nishimura SY, Brasselet S, Moerner WE, McConnell HM (2002). Translational diffusion of individual class II MHC membrane proteins in cells. Biophys J 83, 2681–2692.

Vrljic M, Nishimura SY, Moerner WE, McConnell HM (2005). Cholesterol depletion suppresses the translational diffusion of class II major histocompatibility complex proteins in the plasma membrane. Biophys J 88, 334–347.